Monthly Notices of the ROYAL ASTRONOMICAL SOCIETY

MNRAS **538,** 11–30 (2025) https://doi.org/10.1093/mnras/staf228
Advance Access publication 2025 February 10

Self-regulation of high-redshift black hole accretion via jets: challenges for SMBH formation

Kung-Yi Su,[1]★ Greg L. Bryan [2] and Zoltán Haiman[2]

[1]*Black Hole Initiative, Harvard University, 20 Garden Street, Cambridge, MA 02138, USA*
[2]*Department of Astronomy, Columbia University, 550 West 120th Street, New York, NY 10027, USA*

Accepted 2025 January 31. Received 2025 January 8; in original form 2024 September 17

ABSTRACT

The early growth of black holes (BHs) in atomic-cooling haloes is likely influenced by feedback on the surrounding gas. While the effects of radiative feedback are well-documented, mechanical feedback, particularly from active galactic nucleus (AGN) jets, has been comparatively less explored. Building on our previous work that examined the growth of a 100 $M_\odot$ BH in a constant density environment regulated by AGN jets, we expand the initial BH mass range from 1 to 10^4 $M_\odot$ and adopt a more realistic density profile for atomic-cooling haloes. We reaffirm the validity of our analytic models for jet cocoon propagation and feedback regulation. We identify several critical radii – namely, the terminal radius of jet cocoon propagation, the isotropization radius of the jet cocoon, and the core radius of the atomic-cooling halo – that are crucial in determining BH growth given specific gas properties and jet feedback parameters. In a significant portion of the parameter space, our findings show that jet feedback substantially disrupts the halo's core during the initial feedback episode, preventing BH growth beyond 10^4 $M_\odot$. Conversely, conditions characterized by low jet velocities and high gas densities enable sustained BH growth over extended periods. We provide a prediction for the BH mass growth as a function of time and feedback parameters. We found that, to form a supermassive BH ($> 10^6$ $M_\odot$) within 1 Gyr entirely by accreting gas from an atomic-cooling halo, the jet energy feedback efficiency must be $\lesssim 10^{-4}\dot{M}_{\rm BH}c^2$ even if the seed BH mass is 10^4 $M_\odot$.

Key words: accretion, accretion discs – black hole physics – hydrodynamics – methods: numerical – galaxies: jets.

1 INTRODUCTION

Active galactic nucleus (AGN) feedback is a crucial factor in the evolution of galaxies, particularly in the suppression of star formation in massive galaxies and clusters, thus maintaining their 'red and dead' status for a substantial part of cosmic history. Research extensively indicates that AGN jet feedback mechanisms are theoretically able to quench star formation and arrest cooling flows within galaxy-scale simulations (e.g. Dubois et al. 2010; Gaspari, Brighenti & Temi 2012; Yang, Sutter & Ricker 2012; Li & Bryan 2014; Li et al. 2015; Prasad, Sharma & Babul 2015; Yang & Reynolds 2016; Bourne & Sijacki 2017; Ruszkowski, Yang & Zweibel 2017; Su et al. 2020). Observational data also support the notion that AGNs can provide energy outputs on par with cooling rates (Bîrzan et al. 2004). Moreover, AGNs are observed ejecting gas from galaxies, contributing thermal energy through shocks, sound waves, photoionization, Compton heating, or by enhancing turbulence in the circumgalactic medium (CGM) and intracluster medium (ICM), leading to the formation of hot plasma 'bubbles' with significant relativistic components around massive galaxies (see, e.g. Fabian 2012; Hickox & Alexander 2018, for a detailed review). In Su et al. (2021, 2023a), a comprehensive parameter study on AGN jets within $10^{12} - 10^{15}$$M_\odot$ clusters identified certain models that can produce a sufficiently large cocoon with an extended cooling period, enabling these jets to effectively quench the galaxy.

Beyond the established instances of supermassive black holes (SMBHs) in large galaxies, the influence of AGN feedback extends to smaller dwarf galaxies and stellar-mass to intermediate-mass BHs (IMBHs) with masses ranging from $M_{\rm BH}$ ∼a few to $10^5$$M_\odot$ (e.g. Nyland et al. 2017; Bradford et al. 2018; Penny et al. 2018; Dickey et al. 2019; Manzano-King, Canalizo & Sales 2019). These smaller BHs, some of which are the sources of AGN jets, have been observationally documented (e.g. Greene, Ho & Ulvestad 2006; Wrobel & Ho 2006; Wrobel et al. 2008; Mezcua & Lobanov 2011; Nyland et al. 2012; Reines & Deller 2012; Webb et al. 2012; Mezcua et al. 2013a, b; Reines et al. 2014; Mezcua et al. 2015, 2018a, b; Mezcua, Suh & Civano 2019; Reines et al. 2020). It should not be surprising that AGN feedback impacts the development of these smaller BHs, modifying the characteristics of the surrounding gas and significantly influencing their host galaxies, particularly in dwarf and early universe galaxies (e.g. Barai & de Gouveia Dal Pino 2019; Koudmani et al. 2019; Sharma et al. 2020).

Studies have identified SMBH ($M_{\rm BH} > 10^6$ $M_\odot$) in the early universe ($z \gtrsim 4$), with indications of AGN jets (e.g. Sbarrato et al. 2021, 2022). Moreover, recent observations with *JWST* have identified a significant population of SMBHs at relatively high redshifts, beyond $z \sim 6$ and even beyond $z \sim 10$ (e.g. Carnall et al. 2023; Harikane

★ E-mail: kungyisu@gmail.com

et al. 2023; Kocevski et al. 2023; Larson et al. 2023; Onoue et al. 2023; Übler et al. 2023; Maiolino et al. 2024; Scoggins & Haiman 2024). The feasibility of a stellar-mass $\lesssim 100\,M_\odot$ BH or even a direct-collapse BH $\gtrsim 10^4\,M_\odot$ evolving into a SMBH in such a brief time-frame remains uncertain (e.g. Pacucci et al. 2023; Schneider et al. 2023; Bennett et al. 2024; Mehta, Regan & Prole 2024). Specifically, the influence of jets on the growth rate of initial BH seeds poses additional questions regarding their accretion and expansion (e.g. Park & Ricotti 2011; Ryu et al. 2016). The necessity for alternative mechanisms, such as runaway mergers (e.g. Portegies Zwart & McMillan 2002; Gürkan, Freitag & Rasio 2004; Shi, Grudić & Hopkins 2021), primordial BHs, or other strategies to account for the presence of SMBHs in the early universe remains a significant area of inquiry (see Inayoshi, Visbal & Haiman 2020, for a comprehensive review).

Previous research has tackled comparable issues, using various feedback mechanisms, including radiation (e.g. Milosavljević et al. 2009; Park & Ricotti 2011) and stellar winds (e.g. Takeo, Inayoshi & Mineshige 2020), or by studying the development of slightly larger BHs ($> 10^4\,M_\odot$) through simulations at the scale of entire galaxies with jet feedback (e.g. Regan et al. 2019; Massonneau et al. 2022). In the study presented in Su et al. (2023b), we explored the influence of AGN jets on the accretion processes of BHs with masses of $100\,M_\odot$ located in dense, low-metallicity gaseous environments typical of the cores of atomic-cooling haloes. Additionally, we examined the dynamics of how jet-induced cocoons expand across extensive radii. Our methodology involved a systematic variation of parameters such as gas density, temperature, and the AGN feedback mechanism to ascertain the dependency of BH accretion rates and jet propagation characteristics on these factors.

Our approach in that work involved modelling the gas environment surrounding BHs at resolutions exceeding the Bondi radius, enabling accurate estimation of the gravitational capture of gas particles. Starting from Su et al. (2023b), we employed a variety of jet models to investigate their influence on the growth of BHs and the outward propagation of jets. Through that research, we developed an analytical model that aligned with our simulation outcomes, offering insights into jet propagation and the self-regulation mechanisms of AGN fluxes and BH accretion rates. Moreover, we predicted conditions under which super-Eddington accretion occurs. Yet, that model has limitations, being only validated in simulations with initially static gas environments and at a $100\,M_\odot$ BH mass. Indeed, as a BH accrues mass, the assumption of constant density up to the Bondi radius becomes increasingly unrealistic within the typical size of an atomic-cooling halo. Building on this previous effort (Su et al. 2023b), this study broadens our exploration to include a wider array of BH seed masses from stellar-mass to the lower mass end of direct-collapse BH range (1–$10^4\,M_\odot$). We also included a more realistic density profile resembling the core of an atomic-cooling halo.

In Section 2, we summarize our initial conditions (ICs), BH accretion model, and the AGN jet parameters we survey, as well as describe our numerical simulations. In Section 3, we outline the toy model that describes jet propagation and self-regulation in a constant-density environment. We present the simulation results in Section 4. We then generalize the toy model to include cases where the jet cocoon propagates into a decaying density profile and further suppresses the gas density in Section 5. Based on the toy model, we predict the BH mass as a function of time, seed BH mass, feedback mass loading, and jet velocity in Section 6. We discuss the limitations of the work and its observational implications in Section 7. Finally, we summarize our main conclusion in Section 8.

2 METHODOLOGY

Our study involves conducting simulations on a gas box influenced by jet feedback from a $100\,M_\odot$ BH, utilizing the GIZMO code[1] (Hopkins 2015) in its meshless finite mass (MFM) configuration. This method combines the strengths of grid-based and smoothed-particle hydrodynamics (SPH) techniques in a Lagrangian mesh-free Godunov approach. We detail the numerical implementation and conduct thorough tests, as described in methodological papers focussing on hydrodynamics and self-gravity (Hopkins 2015). Our simulations incorporate the FIRE-2 model for cooling processes (ranging from 10 to 10^{10} K), encompassing photoelectric and photoionization heating, along with collisional, Compton, fine structure, recombination, atomic, and molecular cooling effects. We set a lower limit for the temperature, T_∞, defined in the initial conditions, to prevent the gas from cooling below this threshold due to other feedback mechanisms not covered in our simulations. In the absence of such a limit, and considering the densities in our study, molecular cooling could reduce the temperature of all gas to 10 K in less than 1000 yr, even at extremely low metallicity levels ($10^{-4}\,Z_\odot$ in this case).

2.1 Initial conditions

In an optimal setting, we would model BH accretion within a cosmological simulation that precisely resolves gas dynamics at early cosmic times, similar to studies conducted on minihaloes (Alvarez, Wise & Abel 2009). However, due to significant uncertainties in the conditions at high redshifts, and in order to gain a better understanding of the physics, we adopt a simplified approach that simulates the environment near the BH as a uniform gas patch, akin to the core of an atomic-cooling halo. We systematically vary the properties of this gas patch to explore their influence on BH regulation. Our initial set-up is a 3D box populated with randomly placed gas particles at a fixed temperature, denoted as T_∞. The gas density initially adheres to a specific profile as outlined in Table 1. For simulations with BHs less than $100\,M_\odot$, the density ($n_{\rm Bondi}$) is constant throughout. In cases involving a $10^4 M_\odot$ BH, the density is uniform up to the Bondi radius ($n_{\rm Bondi}$), beyond which it follows a power-law distribution, $n \propto r^\alpha$, as per Regan et al. (2019). A BH occupies the centre of the set-up, with the gas's initial metallicity being set at a very low level ($10^{-4}\,Z_\odot$). All elements in the initial set-up are dynamic, evolving in response to gravitational, hydrodynamic, and additional baryonic physics.

To attain enhanced resolution near the BH, crucial for capturing the dynamics of accretion and feedback processes, we implement a hierarchical super-Lagrangian refinement technique (Su et al. 2020, 2021). This strategy enables us to achieve a superior mass resolution in the area surrounding the z-axis, where the jet originates, as outlined in Table 1, significantly exceeding the resolution achieved in many earlier global investigations. The resolution progressively decreases with distance from the z-axis ($r_{\rm 2d}$), in a manner approximately proportional to $r_{\rm 2d}$. These computational specifics are comprehensively documented in Table 1. Insights from our resolution analysis are detailed in the appendix of Su et al. (2023b).

[1]A public version of this code is available at http://www.tapir.caltech.edu/~phopkins/Site/GIZMO.html.

Table 1. Physics variations of all simulations.

Model	Numerical details					Feedback parameters			Background gas			Resulting averaged accretion rate and fluxes			
	$M_{\rm BH}$	ΔT	Box size	$m_{\rm g}^{\rm max}$	$m_{\rm jet}$	$\eta_{\rm m,fb}$	$V_{\rm jet}$	$T_{\rm jet}$	$n_{\rm Bondi}$	$n_{\rm index}$	T_∞	$\langle\dot{M}_{\rm BH}\rangle$	$\frac{\langle\dot{M}_{\rm BH}\rangle}{\dot{M}_{\rm Bondi}}$	$\frac{\langle\dot{M}_{\rm BH}\rangle}{\dot{M}_{\rm Edd}}$	$\frac{\langle\dot{E}_{\rm jet}\rangle}{\dot{E}_{\rm Edd}}$
	$M_\odot$	kyr	pc	$M_\odot$	$M_\odot$		km s^{-1}	K	cm^{-3}		K	$M_\odot$ yr^{-1}			
1 $M_\odot$															
Fiducial															
m1-η5e-1–vj1e4–n1e5–T1e4	1	1	0.004	1.4e-12	1e-13	0.5	1e4	1e4	1e5	0	6e3	4.7e-13	1.4e-4	2.1e-5	5.9e-8
Jet velocity and FB mass fraction															
m1-η5e-1–vj3e3–n1e5–T1e4	1	1	0.004	1.4e-12	1e-13	0.5	3e3	1e4	1e5	0	6e3	7.9e-12	2.4e-3	3.5e-4	8.9e-8
m1-η1e2–vj3e3–n1e5–T1e4	1	1	0.004	1.4e-12	1e-13	100	3e3	1e4	1e5	0	6e3	2.5e-14	7.7e-6	1.1e-6	5.6e-8
m1-η5e-2–vj1e4–n1e5–T1e4	1	1	0.004	1.4e-12	1e-13	0.05	1e4	1e4	1e5	0	6e3	1.8e-12	5.6e-4	8.3e-5	2.3e-8
m1-η1e2–vj1e4–n1e5–T1e4	1	1	0.004	1.4e-12	1e-13	100	1e4	1e4	1e5	0	6e3	2.9e-15	9.1e-7	1.3e-7	7.4e-8
m1-η5e-2–vj3e4–n1e5–T1e4	1	1	0.004	1.4e-12	1e-13	0.05	3e4	1e4	1e5	0	6e3	5.7e-13	1.7e-4	2.5e-5	6.4e-8
m1-η5e-1–vj3e4–n1e5–T1e4	1	1	0.004	1.4e-12	1e-13	0.5	3e4	1e4	1e5	0	6e3	6.1e-14	1.9e-5	2.7e-6	6.9e-8
Gas density															
m1-η5e-2–vj1e4–n1e2–T1e4	1	1	0.004	1.4e-15	1e-16	0.05	1e4	1e4	1e2	0	6e3	8.1e-16	2.5e-4	3.7e-8	1.0e-11
m1-η5e-2–vj1e4–n1e3–T1e4	1	1	0.004	1.4e-14	1e-15	0.05	1e4	1e4	1e3	0	6e3	1.1e-14	3.3e-4	4.8e-7	1.3e-10
m1-η5e-1–vj1e4–n1e4–T1e4	1	1	0.004	1.4e-13	1e-14	0.5	1e4	1e4	1e4	0	6e3	3.7e-14	1.1e-4	1.7e-6	4.6e-9
m1-η5e-1–vj1e4–n1e6–T1e4	1	1	0.008	1.4e-11	1e-12	0.5	1e4	1e4	1e6	0	6e3	8.0e-12	2.4e-4	3.6e-4	1.0e-6
Temperature															
m1-η5e-1–vj1e4–n1e5–T1e3	1	1	0.032	1.4e-12	1e-13	0.5	1e4	1e3	1e5	0	6e2	1.7e-13	3.7e-6	7.6e-6	2.1e-8
m1-η5e-1–vj1e4–n1e5–T1e5	1	0.16	0.0004	1.4e-12	1e-16	0.5	1e4	1e3	1e5	0	6e4	3.6e-14	2.3e-3	1.6e-6	4.5e-9
100 $M_\odot$															
Fiducial															
m100-η5e-2–vj1e4–n1e5–T1e4 (I,II,III)*	100	100	0.4	1.4e-6	1e-7	0.05	1e4	1e4	1e5	0	6e3	0.7-1.5e-7	2.1-4.6e-3	0.031-0.067	0.87-1.9e-5
Jet velocity															
m100-η5e-2–vj3e3–n1e5–T1e4	100	90	0.8	1.4e-6	1e-7	0.05	3e3	1e4	1e5	0	6e3	1e-5	0.31	4.5	1.1e-4
m100-η5e-2–vj3e4–n1e5–T1e4	100	100	0.4	1.4e-6	1e-7	0.05	3e4	1e4	1e5	0	6e3	8.9e-9	2.7e-4	4.0e-3	1e-5
Gas density															
m100-η5e-2–vj3e3–n1e2–T1e4	100	100	0.4	1.4e-9	1e-10	0.05	1e4	1e4	1e2	0	6e3	1.6e-11	4.9e-4	7.2e-6	2e-9
m100-η5e-2–vj3e3–n1e3–T1e4	100	100	0.4	1.4e-8	1e-9	0.05	1e4	1e4	1e3	0	6e3	2.3e-10	7.0e-4	1.0e-4	2.9e-8
m100-η5e-2–vj3e3–n1e4–T1e4	100	100	0.4	1.4e-7	1e-8	0.05	1e4	1e4	1e4	0	6e3	3.5e-9	1.1e-3	1.6e-3	4.4e-7
m100-η5e-2–vj3e3–n1e6–T1e4	100	40	0.8	1.4e-5	1e-6	0.05	1e4	1e4	1e6	0	6e3	1.3e-5	4e-2	5.8	1.6e-3
Gas temperature															
m100-η5e-2–vj3e3–n1e5–T1e3	100	50	3.2	1.4e-6	1e-7	0.05	1e4	1e4	1e5	0	6e3	1.9e-6	4.2e-3	0.85	2.4e-4
m100-η5e-2–vj3e3–n1e5–T1e5	100	12	0.08	1e-8	8e-10	0.05	1e4	1e4	1e5	0	1e5	4.4e-9	6.0e-2	2.0e-3	5.5e-7
10000 $M_\odot$															
Fiducial															
m1e4-η5e-2–vj1e4–n1e5–T1e4	1e4	1e4	1280	5.7e-1	0.04	0.05	1e4	1e4	1e5	−2	6e3	1.2e-2	3.8e-2	5.6e1	1.6e-2
FB mass fraction															
m1e4-η5e-1–vj1e4–n1e5–T1e4	1e4	1e4	1280	5.7e-1	0.04	0.5	1e4	1e4	1e5	−2	6e3	4.5e-3	1.4e-2	2.0e1	5.6e-2
m1e4-η1e2–vj1e4–n1e5–T1e4	1e4	1e4	1280	5.7e-1	0.04	100	1e4	1e4	1e5	−2	6e3	8.8e-6	2.7e-5	4.0e-2	2.2e-2
Jet velocity															
m1e4-η5e-1–vj3e3–n1e5–T1e4	1e4	1100	1280	5.7e-1	0.04	0.5	3e3	1e4	1e5	−2	6e3	1.4e-1	4.1e-1	6.1e2	1.5e-1
m1e4-η5e-1–vj1e5–n1e5–T1e4	1e4	6000	1280	5.7e-1	0.04	0.05	1e5	1e4	1e5	−2	6e3	2.0e-4	6.0e-4	8.8e-1	2.5e-2
Gas density															
m1e4-η5e-2–vj1e4–n1e2–T1e4	1e4	9450	320	1.5e-4	1e-5	0.05	1e4	1e4	1e2	−2	6e3	7.6e-8	2.3e-4	3.4e-4	9.5e-8
m1e4-η5e-2–vj1e4–n1e3–T1e4	1e4	9910	320	1.5e-3	1e-4	0.05	1e4	1e4	1e3	−2	6e3	4.8e-6	1.5e-3	2.2e-2	6.0e-6
m1e4-η5e-2–vj1e4–n1e4–T1e4	1e4	1e4	320	1.5e-2	1e-3	0.05	1e4	1e4	1e4	−2	6e3	2.9e-4	8.8e-3	1.3	3.6e-4

Notes. This is a partial list of simulations studied here with different jet and background gas parameters. The columns list: (1) Model name: the name of each model starts with the BH mass, followed by the feedback mass loading and the jet velocity in km s^{-1}. The final two numbers represent the background gas density in cm^{-3} and the background gas temperature in K. (2) ΔT: simulation duration. We ensured a run-time of at least 10 times the free-fall time at the Bondi radius, which was sufficient to achieve a semisteady state. (3) Box size of the simulation. (4) $m_{\rm g}^{\rm max}$: the highest mass resolution. (5) $m_{\rm jet}^{\rm max}$: the mass resolution of the spawned jet particles. (6) $\eta_{\rm m,fb}$: the feedback mass loading. (7) $V_{\rm jet}$: the initial jet velocity at spawn. (8) $T_{\rm jet}$: the initial jet temperature at spawn. (9) n_∞: the background gas density. (10) T_∞: the background gas temperature. (11) $\langle\dot{M}_{\rm BH}\rangle$: the resulting time-averaged accretion rate. (12) $\langle\dot{M}_{\rm BH}\rangle/\dot{M}_{\rm Bondi}$: the same value over the Bondi accretion rate. (13) $\langle\dot{M}_{\rm BH}\rangle/\dot{M}_{\rm Edd}$: the same value over the Eddington accretion rate ($\dot{M}_{\rm Edd}\equiv\dot{L}_{\rm Edd}/0.1c^2$). (14) $\langle\dot{E}_{\rm jet}\rangle/\dot{L}_{\rm Edd}$: jet energy flux over the Eddington luminosity.

* We have run three variations of the same run with different random seeds (labelled as I, II, III) to characterize numerical stochasticity. If not specified in the rest of this paper, we are referring to run I.

2.2 Black hole accretion

As highlighted in the introduction, our approach to modelling BH accretion diverges from the conventional Bondi assumption, favoring a method that simulates the gravitational capture of gas directly on to the BH, feeding a subgrid α-disc (Torrey et al. 2020). A gas particle is designated for accretion if it is gravitationally bound to the BH and its estimated pericentric radius is less than the sink radius, $r_{\rm acc}$. This sink radius is defined as $3\times10^{-5}-1.5\times10^{-4}\left(m_g^{\rm max}/1.4\times10^{-6}\right)^{-1/3}$ pc, tailored to the gas density in the vicinity of the BH. $m_g^{\rm max}$ represents the maximum gas mass resolution for each run, as labelled in Table 1. More specifically, the sink radius $r_{\rm acc}$ is determined as the radius around the BH that encloses 96 'weighted' neighbour-hood gas particles, but with the constraint that it must lie within $3\times10^{-5}-1.5\times10^{-4}\left(m_g^{\rm max}/1.4\times10^{-6}\right)^{-1/3}$ pc.

While our simulations track gas movements in close proximity to the BH, we do not explicitly simulate the accretion disc's detailed physics. Instead, we employ a subgrid α-disc model. Within this model, gas that is accreted contributes to the mass of the α-disc (M_α), which starts at zero. The mass accumulated in the α-disc is then transferred to the BH at a rate determined by the equation

$$\dot{M}_{\rm acc}=M\alpha/t_{\rm disc}, \tag{1}$$

where $t_{\rm disc}$ set to a constant value. This duration is based on the viscous time-scale of a disc as described by Shakura & Sunyaev (1973), assuming the disc temperature is 10^4K. The formula for $t_{\rm disc}$ is derived as $t_{\rm disc}\sim t_{\rm ff}\mathcal{M}^2/\alpha\sim 1000{\rm yr}\,(M_{\rm BH}/100{\rm M}_\odot)\,(\alpha/0.1)^{-1}\left(r_{\rm acc}/10^{-4}{\rm pc}\right)^{1/2}$, where $t_{\rm ff}$ denotes the free-fall time at $r_{\rm acc}$, and $\mathcal{M}$ represents the Mach number. In the appendix of Su et al. (2023b), we delve into the effects of altering $t_{\rm disc}$ on the simulation outcomes. We also briefly discuss in Section 7.2.

2.3 Jet models

We implement a jet model as outlined in Su et al. (2021, 2023b, 2024) and Weinberger et al. (2023) which involves a particle spawning technique for jet launch. This technique generates new gas cells (resolution elements) to simulate jet material, endowing these cells with pre-determined mass, temperature, and velocity to define the jet's specific energy. This approach grants us enhanced control over jet characteristics, as it minimizes dependence on surrounding gas conditions through neighbour-finding algorithms.[2] It also allows for the enforcement of higher resolution within jet structures, facilitating the precise simulation of light jets.

The resolution of the spawned gas particles is given in Table 1. These particles are restricted from merging back into larger gas elements until their velocity drops below 10 per cent of the initial launch speed. To ensure exact conservation of linear momentum, two particles are simultaneously emitted in opposite directions along the z-axis each time the accumulated mass flux of the jet doubles the mass of a target spawned particle. The initial positioning of these particles is random, within a sphere of radius r_0, which is the lesser of $10^{-5}\left(m_g^{\rm max}/1.4\times10^{-6}\right)^{-1/3}$ pc or half the distance from the BH to the nearest gas particle.

For a particle initialized at coordinates (r_0,θ_0,ϕ_0) within a jet model with an opening angle $\theta_{\rm op}=1^o$, the initial velocity direction is adjusted to $2\theta_{\rm op}\theta_0/\pi$ for $\theta_0<\pi/2$ and to $\pi-2\theta_{\rm op}(\pi-\theta_0)/\pi$ for $\theta_0>\pi/2$. This configuration ensures that the trajectories of any two particles will not cross, maintaining a coherent jet structure.

We define the jet mass flux using a fixed feedback mass loading as follows:

$$\dot{M}_{\rm jet}=\eta_{\rm m,fb}\dot{M}_{\rm BH}, \tag{2}$$

which allows us to calculate the feedback energy and momentum fluxes of the jet through the equations:

$$\begin{aligned}\dot{E}_{\rm jet}&=\eta_{\rm m,fb}\dot{M}_{\rm BH}\left(\frac{1}{2}V_{\rm jet}^2+\frac{3kT}{2\mu}\right),\\ \dot{P}_{\rm jet}&=\eta_{\rm m,fb}\dot{M}_{\rm BH}V_{\rm jet},\end{aligned} \tag{3}$$

where $V_{\rm jet}$ represents the chosen velocity for the jet, and μ signifies the average mass of a jet particle.

The efficiency jet energy efficiency is

$$\eta_{\rm eff}\equiv\frac{\dot{E}_{\rm jet}}{\dot{M}_{\rm BH}c^2}=\frac{\eta_{\rm m,fb}V_{\rm jet}^2}{2c^2}+\frac{\eta_{\rm m,fb}3kT}{2\mu c^2}. \tag{4}$$

We note that the jet's mass loading and velocity depends on various factors in the vicinity of the BH, including the properties of the accretion disc and the BH spin. However, uncertainties persist regarding how feedback propagates from the event horizon scale to the scales resolvable in our simulations. To address this, we opted for a series of runs varying the feedback mass loading and velocity as free parameters, rather than introducing a more sophisticated functional dependence of feedback efficiency. This approach allows us to gain a clearer understanding of BH growth as a function of these parameters, which may realistically not be free.

3 REVIEW OF A SIMPLE MODEL FOR JET PROPAGATION AND COCOON FORMATION

In Su et al. (2023b), we developed a toy model describing the jet propagation and feedback regulation. We briefly summarize it here for future verification over a wider BH mass range (and modification for a non-uniform background in Section 5).

3.1 Jet propagation

When a jet is launched, the initial cocoon (defined here as the outer shock) can be approximately described by a cylindrical expansion, with width and height $R_{\rm cocoon}(t)$ and $Z_{\rm cocoon}(t)$. The cocoon evolution follows from momentum conservation in the z-direction and energy consideration in the lateral directions (e.g. Begelman & Cioffi 1989; Su et al. 2021). With this, we can write down the propagation of the jet cocoon propagating into a background medium with density ρ_∞ as a function of time, as follows:

$$\begin{aligned}V_R(t)&=\left(\frac{\gamma^2}{72\pi\beta^2}\right)^{1/6}\dot{M}_{\rm jet}^{1/6}\rho_c^{1/6}\rho_\infty^{-1/3}V_{\rm jet}^{1/2}t^{-1/3}\\ R_{\rm cocoon}(t)&=\left(\frac{81\gamma^2}{512\pi\beta^2}\right)^{1/6}\dot{M}_{\rm jet}^{1/6}\rho_c^{1/6}\rho_\infty^{-1/3}V_{\rm jet}^{1/2}t^{2/3}\end{aligned} \tag{5}$$

and the time dependence of V_z and $z_{\rm cocoon}$ as

$$\begin{aligned}V_z(t)&=\left(\frac{8\beta}{9\pi\gamma}\right)^{1/3}\dot{M}_{\rm jet}^{1/3}\rho_c^{-1/6}\rho_\infty^{-1/6}t^{-2/3}\\ z_{\rm cocoon}(t)&=\left(\frac{24\beta}{\pi\gamma}\right)^{1/3}\dot{M}_{\rm jet}^{1/3}\rho_c^{-1/6}\rho_\infty^{-1/6}t^{1/3},\end{aligned} \tag{6}$$

[2]Conventionally, energy and momentum are distributed to gas particles identified via a neighbour search from the BH, making the impact reliant on local gas attributes and their spatial arrangement. Refer to Wellons et al. (2022) for a discussion on various methodologies.

where $\gamma \equiv \dot{E}_{\rm expansion}/\dot{E}_{\rm kin} \propto \dot{E}_{\rm jet}/\dot{E}_{\rm kin} \equiv f_{\rm kin}^{-1}$, β is an order-of-unity factor accounting for the non-cylindrical shape of the jet cocoon, and ρ_c is the cocoon gas density. Assuming the jet results in strong shocks, γ in the above expression roughly follows:

$$\begin{aligned}\gamma_{\rm super-sonic} &\sim \frac{\dot{E}_{\rm post-shock}}{\dot{E}_{\rm pre-shock}} \frac{\dot{E}_{\rm pre-shock}}{\dot{E}_{\rm jet}} \frac{\dot{E}_{\rm jet}}{\dot{E}_{\rm kin}} \\ &\sim \frac{\rho_{\rm post} v_{\rm post}^3}{\rho_{\rm pre} v_{\rm pre}^3} \times (1 - f_{\rm loss}) f_{\rm kin}^{-1} \\ &\sim \frac{1}{16} \times (1 - f_{\rm loss}) f_{\rm kin}^{-1} \lesssim \frac{1}{16} f_{\rm kin}^{-1}, \end{aligned} \tag{7}$$

where $f_{\rm loss}$ represents the fraction of energy lost through radiative cooling during propagation.

We assume that ρ_c, the cocoon gas density, is related to the background gas density and velocity and jet velocity as

$$\rho_c \propto \rho_\infty^\zeta T_\infty^\xi V_{\rm jet}^\delta, \tag{8}$$

where ζ, ξ, and δ are exponents that we will determine later.

Following equations (5) and (6), the lateral size grows more rapidly than the z-expansion and eventually becomes comparable to the propagation distance in the jet direction ($R_{\rm cocoon}/z_{\rm cocoon} \sim 1$). This happens at a height of

$$\begin{aligned} z_{\rm iso} \equiv r_{\rm iso} &= \left(\frac{\dot{M}_{\rm jet}}{2\pi\rho_c V_{\rm jet}}\right)^{1/2} \left(\frac{16\beta}{\gamma}\right) \\ &\approx 1.3 \times 10^{-3} {\rm pc}\ (1 - f_{\rm loss})^{-1} f_{\rm kin} \times \left(\frac{n_c}{10^5\ {\rm cm^{-3}}}\right)^{-1/2} \\ &\left(\frac{\dot{M}_{\rm jet}}{5 \times 10^{-9}\ {\rm M_\odot yr^{-1}}}\right)^{1/2} \left(\frac{V_{\rm J}}{10^4\ {\rm km\ s^{-1}}}\right)^{-1/2}, \end{aligned} \tag{9}$$

where n_c is the gas number density of the cocoon (corresponding to ρ_c). Beyond this radius, the cocoon becomes isotropic, with radius $R(t)$, and the propagation is governed solely by energy conservation with:

$$\begin{aligned} V_{\rm R}(t) &= \left(\frac{9\gamma' \dot{M}_{\rm jet} V_{\rm jet}^2 \rho_c^{1/2}}{200\pi\rho_\infty^{3/2}}\right)^{1/5} (t - t_{\rm iso})^{-2/5} \\ R(t) &= \left(\frac{125\gamma' \dot{M}_{\rm jet} V_{\rm jet}^2 \rho_c^{1/2}}{216\pi\rho_\infty^{3/2}}\right)^{1/5} (t - t_{\rm iso})^{3/5}. \end{aligned} \tag{10}$$

3.2 Feedback self-regulation

In Su et al. (2023b), we concluded that jet feedback self-regulates such that the time-averaged isotropic component of the outflowing momentum flux of the jet cocoon roughly balances the free-fall inflowing momentum flux at the Bondi radius (the 'Bondi flux'). The isotropic component is defined as the radial momentum flux, assuming that the momentum flux in all directions is the minimum of the lateral or the jet-direction components. Depending on where the cocoon isotropizes, there can be two possibilities: one when $r_{\rm iso} > r_{\rm Bondi}$ and one when $r_{\rm iso} < r_{\rm Bondi}$. The resulting mass flux approximately obeys the following expression:

$$\dot{M}_{\rm jet} \sim \begin{cases} \propto M_{\rm BH}^2 \rho_\infty^{2-\zeta}\ T_\infty^{-\xi}\ V_{\rm jet}^{-3-\delta} & ({\rm for}\ r_{\rm iso} > r_{\rm Bondi}) \\ \propto M_{\rm BH}^2 \rho_\infty^{(3-\zeta)/2} T_\infty^{-(1+\xi)/2} V_{\rm jet}^{-2-\delta/2} & ({\rm for}\ r_{\rm iso} < r_{\rm Bondi}) \end{cases} \tag{11}$$

The jet cocoon will be elongated at the Bondi radius if $z_{\rm iso} > r_{\rm Bondi}$ or, from equations (9), if

$$\dot{M}_{\rm jet} > \left(\frac{\pi\gamma^2 r_{\rm Bondi}^2}{128\beta^2}\right) \rho_c V_{\rm jet} \sim \rho_\infty^\zeta\ T_\infty^\xi V_{\rm jet}^{1+\delta}. \tag{12}$$

Otherwise, the cocoon isotropizes before reaching the Bondi radius.

4 SIMULATION RESULTS: A STRONG DEPENDENCE ON BLACK HOLE MASS

We now test (and eventually generalize) these expressions with numerical simulations that push to significantly higher BH masses.

4.1 Black hole accretion and jet fluxes

Fig. 1 shows the BH accretion rate as well as the jet mass, momentum, and energy fluxes for our simulations with varying initial gas densities and BH masses. It is clear that for all BH masses surveyed, jets launched from BHs in denser environments self-regulate to achieve higher mass, momentum, and energy fluxes, all of which increase superlinearly with the density. However, while simulations involving a 10^4 $M_\odot$ BH initially exhibit a similar pattern, the accretion rates and fluxes rapidly decline thereafter. The majority of the BH accretion occurs within the first 2 Myr, after which the contribution to the net accreted mass becomes exponentially small throughout the simulations. As we will discuss in more detail below, this is primarily due to the overall drop in density profiles in some of the runs when the jet cocoon propagates beyond the core radius, approximately 1 pc. We will discuss the conditions for such density suppression and its effects in later sections.

4.2 Agreement with analytic models for black holes up to $M_{\rm BH} < 10^4\ {\rm M_\odot}$

In this work, we survey a broader range of BH masses, from 1 to 10^4 $M_\odot$. As we mentioned in Section 4.1, and will return to later, a suppression of the density profile can occur for $M_{\rm BH} \gtrsim 10^4\ {\rm M_\odot}$. In this section, we show that the analytic models described in Section 3 hold for BHs up to $M_{\rm BH} < 10^4\ {\rm M_\odot}$. The case of $M_{\rm BH} = 100\ {\rm M_\odot}$ was demonstrated in our previous papers, so this section focusses primarily on the $M_{\rm BH} = 1\ {\rm M_\odot}$ cases.

4.2.1 The self-regulation of the cocoon by its isotropic momentum flux

Fig. 2 shows that the regulation found in Su et al. (2023b) also occurs for the smaller BH, $M_{\rm BH} = 1\ {\rm M_\odot}$, which we explicitly tested in this work. In Fig. 2, we plot the injected jet momentum flux (red), the isotropic (pink), and z component (cyan) of the outflowing jet cocoon momentum flux, and the inflowing momentum flux assuming a Bondi solution (green) as a function of radius. Additionally, we indicate the Bondi radius with a vertical grey line.

In the low-jet-velocity ($V_{\rm jet} \sim 3000\ {\rm km\ s^{-1}}$) cases, the jet cocoon clearly manifests momentum conservation in the z direction, as the z component of cocoon momentum flux (cyan) agrees with the injected jet momentum flux (red) to radii beyond the Bondi radius. The isotropic component of the cocoon momentum flux eventually picks up and becomes comparable to the z component of the cocoon momentum flux at the isotropization radius. Beyond this, the propagation of the jet cocoon becomes an energy-driven bubble, and the outflowing cocoon momentum flux can be higher than the injected momentum flux. Although at the Bondi radius the isotropic component of the cocoon momentum flux is much smaller than the z component momentum flux, it is the isotropic component that is regulated to the free-fall inflowing momentum flux at the Bondi radius. The overall picture is consistent with what is described in Section 3.2 for the case where $r_{\rm iso} > r_{\rm Bondi}$.

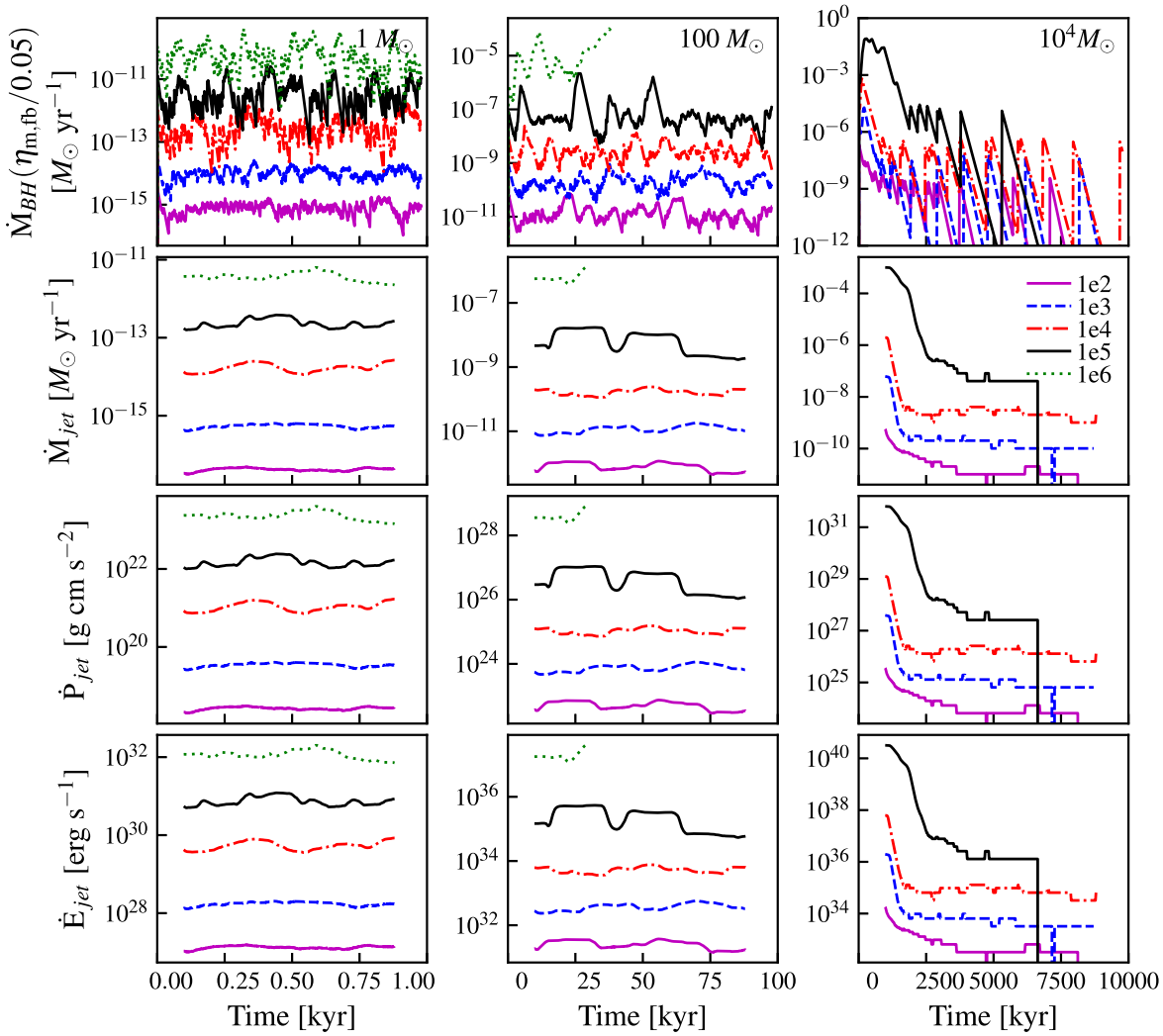

Figure 1. From top to bottom, each row of panels shows (i) the black hole accretion rate, (ii) jet mass flux, (iii) momentum flux, and (iv) energy flux, in runs, varying the initial gas density from 10^2 to 10^6 cm^{-3} (density denoted by line colour and style). The columns show these quantities for initial black hole mass of $1\,M_\odot$ (left), $100\,M_\odot$ (centre), and $10^4\,M_\odot$ (right). The second, third, and fourth rows (from the top) show moving averages around the specific time of the run. Jets emanating from black holes in denser environments self-regulate to achieve higher mass, momentum, and energy flux, all of which increase superlinearly with the density. Simulations involving a $10^4\,M_\odot$ black hole initially exhibit a similar pattern; however, the accretion rates and fluxes rapidly decline thereafter.

For runs with higher jet velocity, this isotropization happens at smaller radii, eventually occurring within the Bondi radius. However, in those cases, it is also the isotropic component of the cocoon momentum flux that matches the inflowing momentum flux, assuming the Bondi value at the Bondi radius. The overall picture is again consistent with what is described in Section 3.2 for the case where $r_{\rm iso} < r_{\rm Bondi}$.

4.2.2 *Thermal phase structure of the cocoon/bubble gas*

To determine how the jet mass flux scales with the gas properties and feedback parameters according to equation (11), we first need to understand how the thermodynamic properties of the cocoon gas scale with those of the background gas (parametrized as power laws in equation 8). Our previous study (Su et al. 2023b) concluded that the scaling roughly follows $n_c \propto n_\infty^\zeta T_\infty^\xi$ with $\zeta \lesssim 0.9$ and $\xi \sim 0$ for $M_{\rm BH} = 100\,M_\odot$.

As we explore a broader range of BH masses, Fig. 3 describes the scaling for $M_{\rm BH} = 1\,M_\odot$. The y-axes represent the cocoon gas density and temperature, while the x-axes represent the background gas temperature and density. The red, blue, and green dots and lines correspond to the hot, cold, and combined phases, respectively. The dots are from each simulation, and the lines are fitted power laws with the index (κ) labelled. For simplicity, the cocoon is defined as all gas with $T > 1.2T_\infty$. We find $n_c \propto n_\infty^\zeta T_\infty^\xi$ with $\zeta \lesssim 0.9$ and $\xi \sim -0.6$ to -0.7.

4.2.3 *The black hole accretion rate and jet mass flux*

With the scaling of gas properties relative to the background gas properties, we now have the full scaling of the BH accretion rate with respect to the jet parameters and the gas properties (following equation equation 11). Fig. 4 shows a comparison of what the toy model predicts versus what we measured in the simulation.

The top four panels in this figure show the results for a $1\,M_\odot$ BH. The scaling obtained from the toy model (indicated in brackets) is broadly comparable to the fitted slope from the simulation.

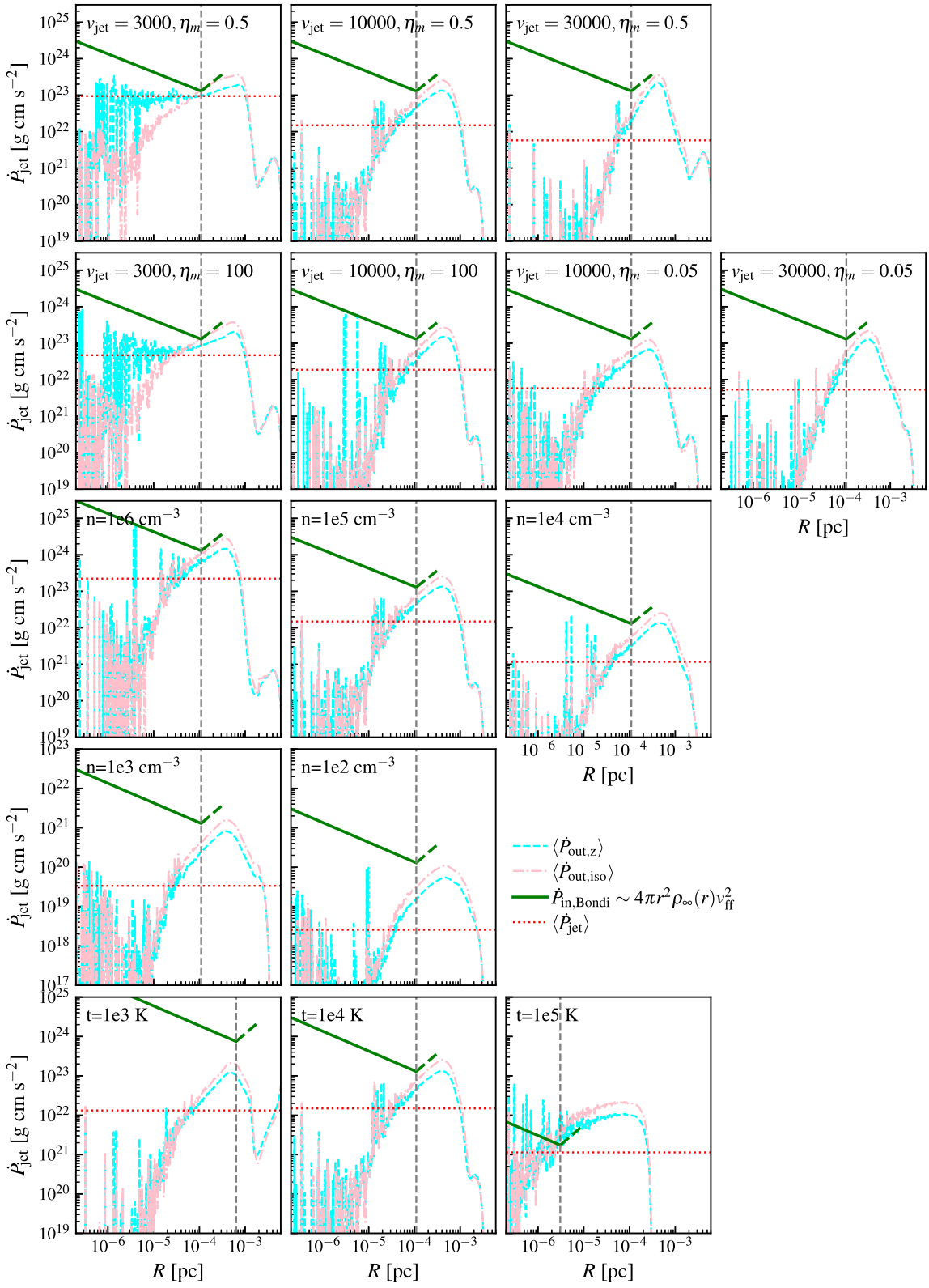

Figure 2. The comparison of time-averaged momentum fluxes from the simulations is shown. Three types of momentum flux are illustrated: (i) the average jet momentum flux (red dotted), (ii) the cocoon momentum flux, with cyan dashed and pink dash-dotted lines representing the z component and the isotropic component (comparable to the lateral component), respectively, and (iii) the estimated inward free-fall (Bondi) momentum flux (green thick). The dashed grey vertical line in each plot indicates the Bondi radius. The isotropic component of the outward cocoon momentum flux matches the inward Bondi momentum flux at the Bondi radius. Runs with elongated cocoons (v = 3000 km s^{-1}) have the z-component of their cocoon fluxes roughly matching the jet momentum fluxes (momentum-driven) and are much larger than the isotropic components. Runs with bubble-shaped cocoons (v$\gtrsim$10000 km s^{-1}, all except for the two panels with v = 3000 km s^{-1}) all exhibit cocoon momentum fluxes (energy-driven) higher than the jet momentum fluxes.

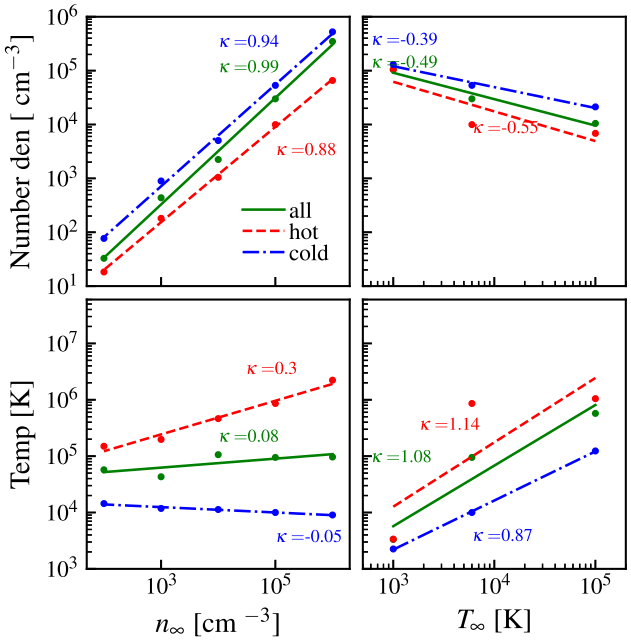

Figure 3. The dependence of the cocoon gas density and temperature on background gas properties (the former evaluated at the Bondi radius) for the $1\,M_\odot$ run is shown. The red, blue, and green dots and lines correspond to the hot, cold, and combined phases, respectively. The dots are from each simulation, and the lines are fitted power laws with the index (κ) labelled. The cocoon is defined for simplicity as all gas with $T > 1.2T_\infty$. We find $n_c \propto n_\infty^\zeta T_\infty^\xi$ with $\zeta \lesssim 0.9$ and $\xi \sim -0.6$ to -0.7.

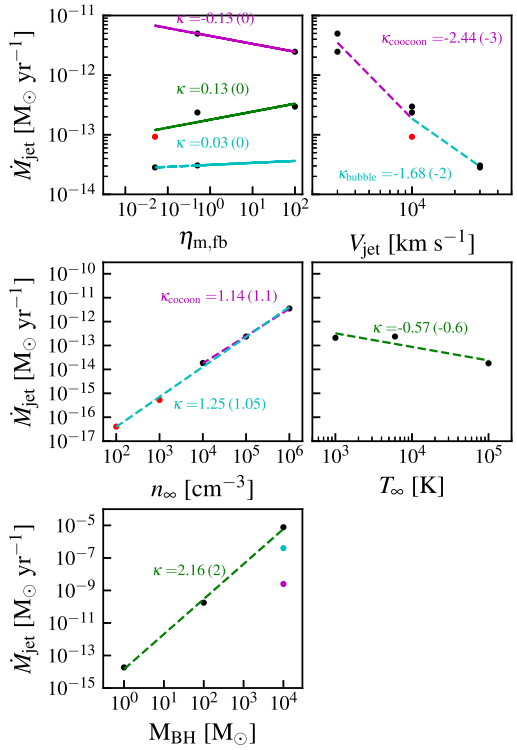

Figure 4. The dependence of the jet mass flux ($\dot{M}_{\rm jet}$) on the adopted jet model and background gas properties is shown for $M_{\rm BH} = 1\,M_\odot$ (top four panels) and across black hole masses assuming $(n_\infty, T_\infty, v_{\rm jet}) = (10^4\,{\rm cm}^{-3}, 10^4\,{\rm K}, 10^4\,{\rm km\,s}^{-1})$ (bottom panel). The black, cyan, and magenta dots, respectively, characterize the accretion rate averaged over the first 0.5 Myr, all time, and after 1 Myr for $M_{\rm BH} = 10^4\,M_\odot$. The dots represent the simulation results, while the lines show power-law fits with the index (κ) labelled. The number in parentheses is an estimate from the toy model, and the fit to the cocoon gas-phase dependence in Fig. 3 roughly agrees with what we measured from the simulation. The red dots represent runs that marginally failed to regulate, hence the slightly lower fluxes. In the last panel for the $10^4\,M_\odot$ case, the black, cyan, and magenta dots represent the accretion rate averaged over the first 0.5 Myr, the entire time, and after 1 Myr, respectively. The later decay in the jet fluxes due to core density suppression is discussed in Section 4.3.

We note that although the toy model predicts the BH accretion rate assuming self-regulation at the Bondi radius, the required mass flux can be too high to achieve this. At any given time, the BH accretion rate and the wind mass flux can, at most, add up to the Bondi accretion flux. If the required fluxes exceed this, the accretion rate is capped at $\dot{M}_{\rm Bondi}\,(1-\eta_{\rm jet,fb})^{-1}$, and the system simply fails to self-regulate. The red dots represent runs that marginally fail to regulate, which makes the fitted slope slightly different from the toy model results.

The bottom panel in Fig. 4 shows the scaling of the BH accretion rate as a function of the BH mass, assuming $n_\infty = 10^4\,{\rm cm}^{-3}$, $T_\infty = 10^4$ K, and $V_{\rm jet} = 10^4\,{\rm km\,s}^{-1}$. The resulting scaling is roughly $\dot{M}_{\rm jet} \sim M_{\rm BH}^2$, consistent with the prediction of the toy model.

We emphasize that we show three points for the $M_{\rm BH} = 10^4\,M_\odot$ case, corresponding to three different times. The black, cyan, and magenta dots, respectively, characterize the accretion rate averaged over the first 0.5 Myr, all time, and after 1 Myr. As time progresses, the accretion rate of the $10^4\,M_\odot$ run decays (see Fig. 1). The lines were fitted only through the black dots (shortest averaging period). The resulting slope indicates that the initial BH accretion and self-regulation are well described by our toy model. Only at later times, when the density profile drops, does the result deviate from the model. We discuss this in the following section, Section 4.3.

4.3 Evolution of density profiles: beyond the $M_{\rm BH} = 10^4\,M_\odot$ threshold

When the BH mass reaches $M_{\rm BH} = 10^4\,M_\odot$, the jet cocoon can propagate beyond the core radius of approximately 1 pc, causing an overall decay of the density profile over time. In this section, we demonstrate this effect.

4.3.1 *The evolution of density profiles*

Fig. 5 shows the time evolution of the density profile for the runs with $M_{\rm BH} = 10^4\,M_\odot$. For all such runs with a density lower than $10^4\,{\rm cm}^{-3}$ and a velocity of $10^4\,{\rm km\,s}^{-1}$ or above, the system experiences density drops over time. As the jet cocoon propagates, this density suppression extends to a larger radius. Eventually, the density suppression stops at approximately 30 pc, which is the terminal radius where the jet cocoon stops propagating (a model for this will be presented in Section 5). Within the terminal radius, the density is roughly uniform. The uniform density can be approximately explained by the high sound speed within the cocoon. Assuming a density profile of $\rho_0(r/r_0)^{-2}$, the resulting uniform density inside the shock front position, R, can be estimated as

$$\langle\rho\rangle \sim \frac{\int_0^R 4\pi r^2 \rho_0 \left(\frac{r}{r_0}\right)^{-2} {\rm d}r}{4\pi R^3/3} \sim 3\rho_0 \left(\frac{R}{r_0}\right)^{-2}. \quad (13)$$

Given that part of the mass is accreted by the BH, this estimate is not far from the original density at the current position of the cocoon's shock front.

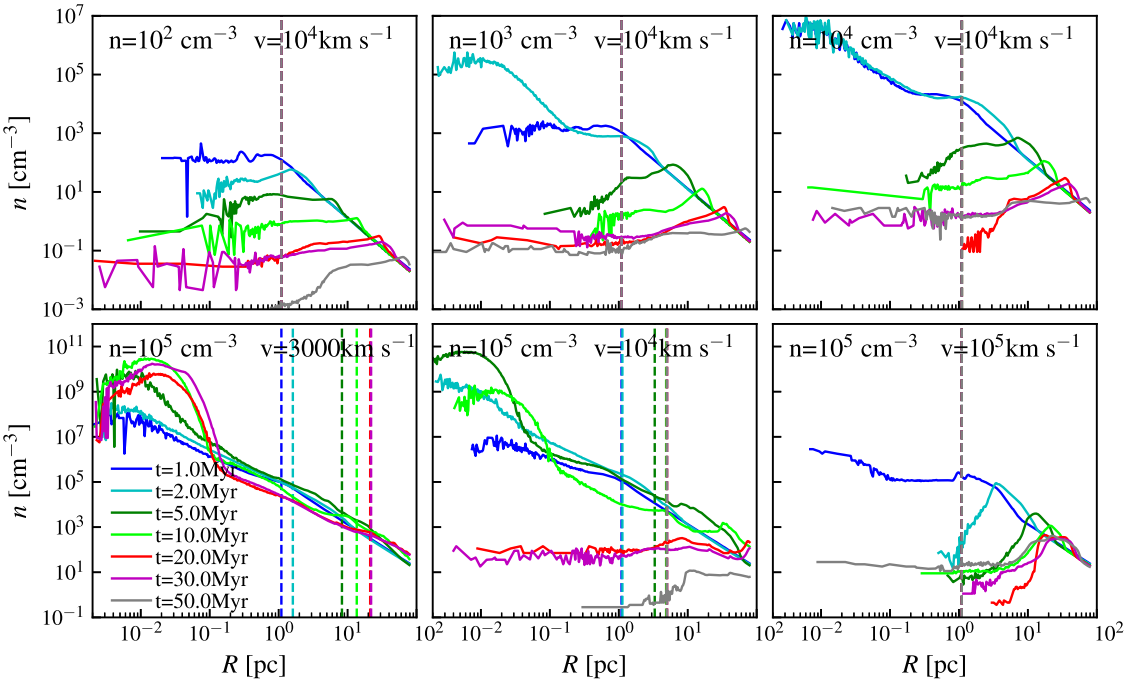

Figure 5. The time evolution of the density profile for the runs with $M_{\rm BH} = 10^4 {\rm M}_\odot$ for a range of jet velocities and core densities (as indicated). For cases with very high jet velocity or a density lower than $10^4\,{\rm cm}^{-3}$, the density within the radius where the cocoon propagates drops to at least the density at the jet cocoon shock front. For the case with $n_\infty = 10^4\,{\rm cm}^{-3}$ and $v_{\rm jet} = 10^4\,{\rm km\,s}^{-1}$, the density profile remains intact until the BH mass grows by a factor of 3, after which the density is suppressed. The density profile remains intact in the low jet velocity case (bottom left panel).

The density suppression also depends on the jet velocity. For higher gas density at $10^5\,{\rm cm}^{-3}$, we tested a wide range of jet velocities. For the fiducial jet velocity of $10^4\,{\rm km\,s}^{-1}$, the density profile is initially sustained at the initial profile for about 100 kyr, during which the BH mass grows by a factor of 3. After that, density suppression starts to occur, and the terminal radius reaches roughly 100 pc. For the lower jet velocity case, density suppression never occurs. Instead, the density evolves from an initially flat profile within the core radius toward a cuspier profile. For the higher jet velocity case, density suppression occurs again.

Overall, the lower the gas density and/or the higher the jet velocity, the more likely density suppression is to happen. The overall trend suggests that the more bubble-like the jet cocoon is, the easier it is for density suppression to occur. We discuss the criteria for this as follows.

4.3.2 Criteria for density suppression

To understand the conditions where density suppression occurs, we highlight three relevant radii: the core radius ($r_{\rm core}$), within which the density is initially flat; the isotropization radius ($r_{\rm iso}$), where the jet cocoon becomes isotropic; and the terminal radius ($r_{\rm terminal}$), where the jet cocoon or bubble stops propagating. Details of the terminal radius are discussed in Section 5. By comparing these three radii, we can identify several different regimes, as characterized in the cartoon shown in Fig. 6. The fourth relevant radius is the Bondi radius ($r_{\rm Bondi}$). If $r_{\rm Bondi}$ falls within the region of suppressed density, the BH 'feels' the density suppression, and the BH accretion rate is reduced. We list them case by case as follows:

(a) $r_{\rm iso} < r_{\rm terminal} < r_{\rm core}$ **(No density suppression)**: as shown in the upper left of Fig. 6, the cocoon stops propagating before reaching the core radius, so it never reaches the radius where the density starts to drop. Therefore, there is no density suppression. This is typical for smaller BH cases ($M_{\rm BH} < 10^4 {\rm M}_\odot$).

(b) $r_{\rm terminal} < r_{\rm iso}$ **(No density suppression)**: as shown in the lower left of Fig. 6, the jet cocoon never isotropizes before losing all its energy. As a result, even if the cocoon penetrates into the low-density region, it does not suppress the density in all directions. Overall, the spherically averaged density profile is not significantly suppressed.

(c) $r_{\rm core} < r_{\rm iso} < r_{\rm terminal}$ **(Density suppression beyond $r_{\rm iso}$)**: as shown in the upper right of Fig. 6, the jet cocoon isotropizes beyond the core radius and continues to propagate into the low-density region. The density then becomes constant from the isotropization radius up to the radius where the jet cocoon shock is. This is typical for more massive BHs ($M_{\rm BH} > 10^4\,{\rm M}_\odot$) with isotropization radius larger than the core radius.

(d) $r_{\rm iso} < r_{\rm core} < r_{\rm terminal}$ **(Density suppression beyond $r_{\rm iso}$)**: as shown in the lower right of Fig. 6, the jet cocoon first isotropizes and then pushes beyond the core radius into the low-density region. As indicated in Fig. 5, the density then becomes constant from the isotropization radius up to the radius of the jet cocoon shock. This is typical for more massive BHs ($M_{\rm BH} > 10^4\,{\rm M}_\odot$) with isotropization radius smaller than the core radius.

4.3.3 The consequence of density suppression – a secularly evolving regulation

As the density profile drops, the density at the Bondi radius also decreases. Meanwhile, the accretion rate and jet fluxes also drop. However, the isotropic component of the outflowing cocoon momentum flux still regulates to the real-time Bondi inflowing momentum flux. The only difference is that it becomes a moving regulation.

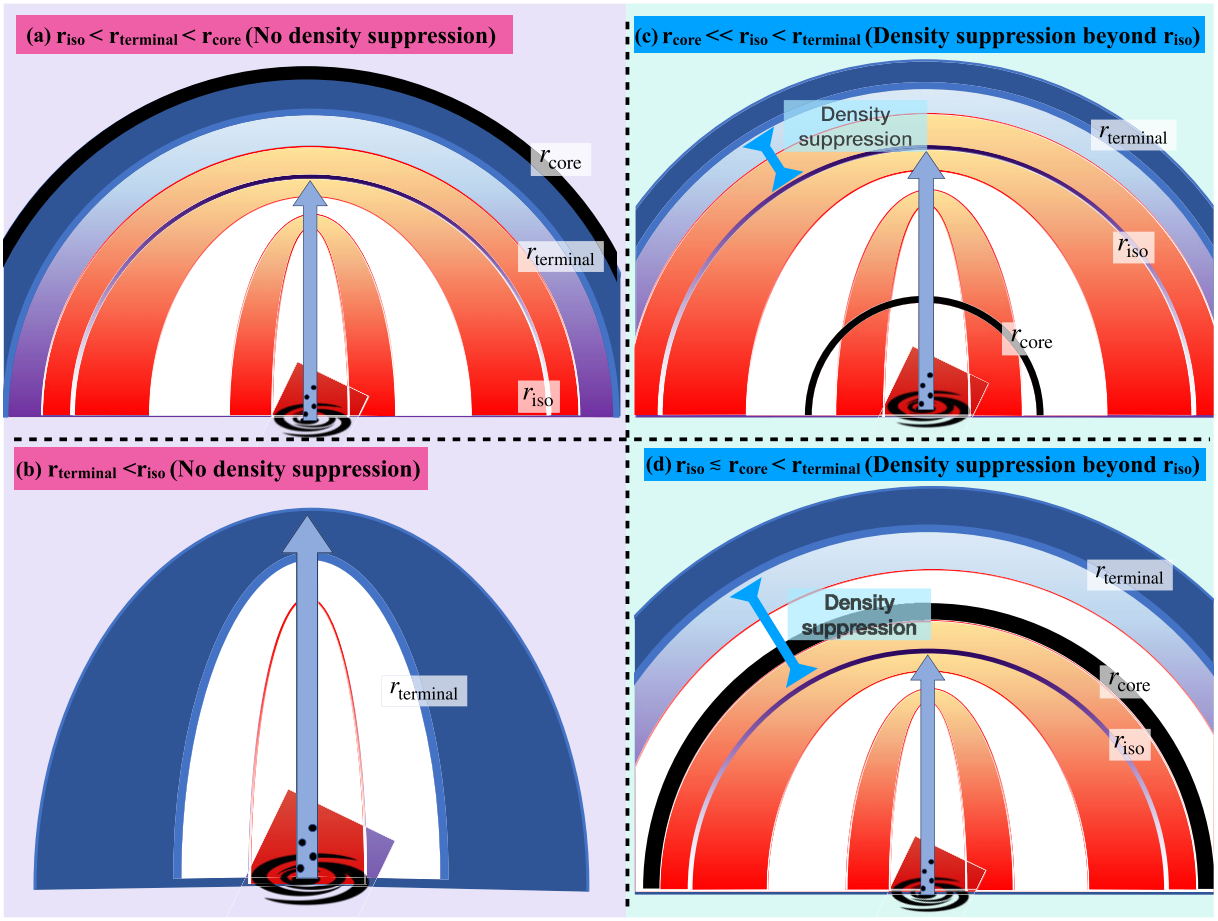

Figure 6. A cartoon depicting the conditions under which an overall drop in the density profile occurs. These conditions are determined by comparing the core radius (r_{core}), within which the density is initially flat; the isotropization radius (r_{iso}), where the jet cocoon becomes isotropic; and the terminal radius ($r_{terminal}$), where the jet cocoon or bubble loses its energy and stalls.

Fig. 7 demonstrates this moving regulation for six different simulations with a $10^4 M_\odot$ BH. As in Fig. 2, we plot the injected jet momentum flux (red), the isotropic (pink), and z component (cyan) of the outflowing jet cocoon momentum flux, and the inflowing momentum flux assuming a Bondi solution based on the initial density (green) as a function of radius. To account for the decay of density at the Bondi radius, we also plotted the Bondi inflowing momentum flux corrected by the real-time measured density at the Bondi radius (lime). We indicate the evolving Bondi radius at each time with a vertical gray line.

Each row represents one run at different times. For all the runs, the real-time corrected Bondi inflowing momentum flux matches the isotropic component of the cocoon momentum flux at the Bondi radius, indicating that this moving regulation holds in a broad sense. We note that the run with $n = 10^5\,\mathrm{cm}^{-3}$, $v = 3000\,\mathrm{km\,s}^{-1}$ (fifth row) never experiences density suppression as time progresses and the BH mass increases. The regulation still holds perfectly.

As the density at the Bondi radius drops, the gas density within the jet cocoon also decreases. Therefore, we need to account for this when determining the scaling relation of cocoon gas density with respect to background gas density (as shown in Fig. 3) for the $M_{BH} = 10^4\,M_\odot$ case. In Fig. 8, we divide the simulation into several 0.1 Myr bins and plot the average background gas density at the Bondi radius (n_{Bondi}) and the cocoon gas density at the Bondi radius (n_{cocoon}) at the corresponding times. As a result of the time-varying regulation, each run forms a series of points, and we fit a line through all the points. We find that $n_{cocoon} \propto n_{Bondi}^{\zeta}$ with $\zeta \lesssim 0.9$, very similar to the scaling relation obtained for other BH masses without the overall density evolution.

Finally, to demonstrate that the toy model picture works even for the moving regulation case, we can plug the scaling relation (between the cocoon gas properties and the background gas properties) into the toy model to obtain the scaling of the BH accretion rate with the background gas properties. Fig. 9 again divides each simulation into 0.8 Myr time periods and calculates the $\dot{M}_{BH}$ and n_{cocoon} averaged over the specific time period. By fitting through all the points, we obtain a scaling relation $\dot{M}_{BH} \propto n_{Bondi}^{1.5}$, broadly similar to (but slightly steeper than) what the toy model implies. The scaling relation is also broadly consistent with what was obtained for the $M_{BH} = 1M_\odot$ and $M_{BH} = 100M_\odot$ cases.

4.4 Summary for the toy model for self-regulation as a function of black hole mass

Here, we summarize what our generalized analytic model predicts for the scalings, and compare it with the simulation results. Compiling the scaling relations we derived, we have:

$$\frac{\dot{M}_{BH}}{\dot{M}_{Edd}} \sim \begin{cases} \propto M_{BH}\rho_\infty^{\alpha_1} T_\infty^{\tau_1} \eta_{m,BH}^{-1} V_{jet}^{-3} & (\text{for } r_{iso} > r_{Bondi}) \\ \propto M_{BH}\rho_\infty^{\alpha_2} T_\infty^{\tau_2} \eta_{m,BH}^{-1} V_{jet}^{-2} & (\text{for } r_{iso} < r_{Bondi}) \end{cases} \quad (14)$$

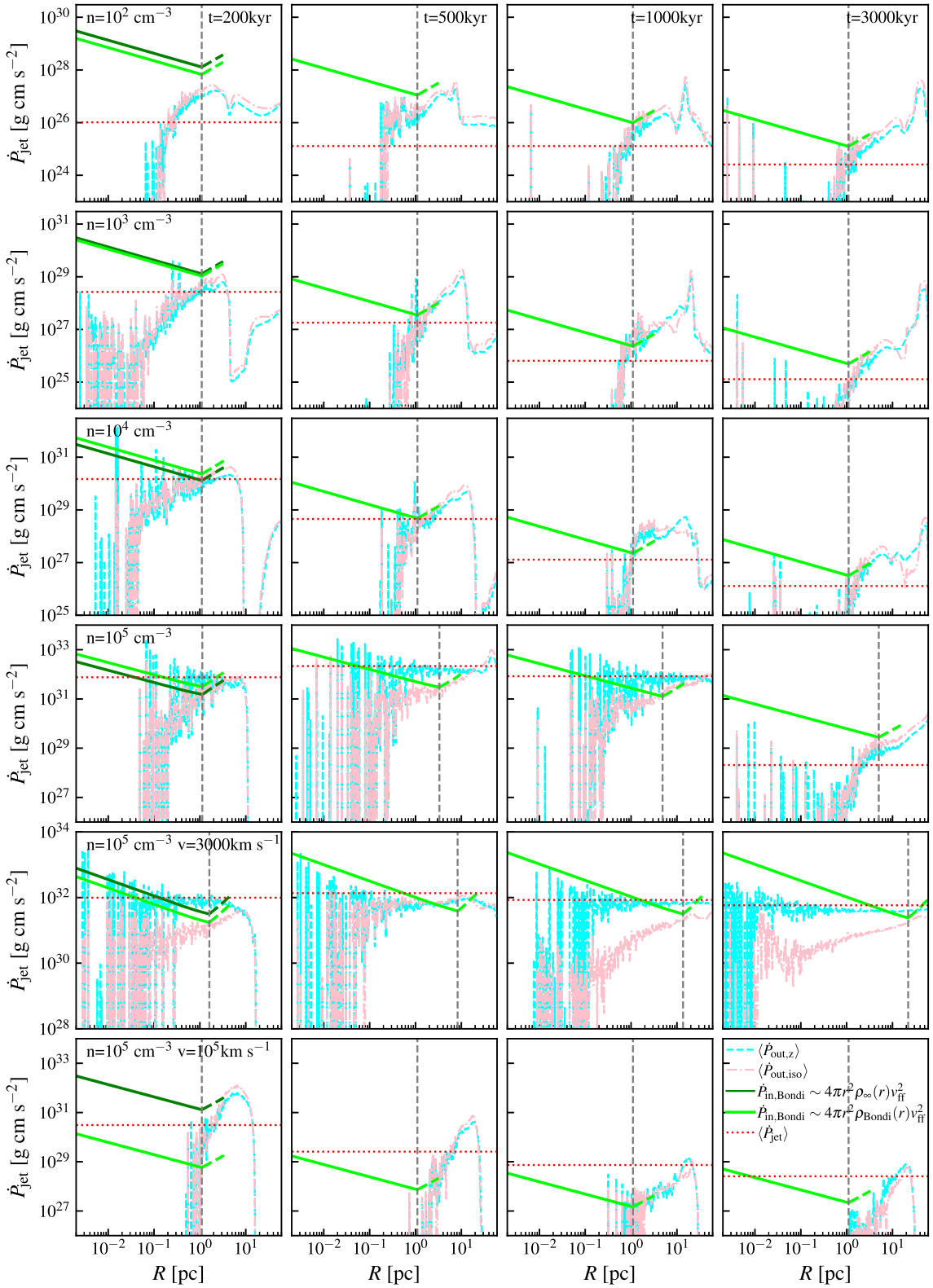

Figure 7. The comparison of time-averaged momentum fluxes from six simulations with $M_{\rm BH} = 10^4 {\rm M}_\odot$. Each row represents one run, with each column corresponding to a different time of that run. Three types of momentum flux are illustrated: (i) the average jet momentum flux (red dotted), (ii) the cocoon momentum flux, with cyan dashed and pink dash-dotted lines representing the z component and the isotropic component (comparable to the lateral component), respectively, and (iii) the estimated inward Bondi momentum flux assuming the initial density (green thick) and real-time density (lime thick). The dashed grey vertical line in each plot indicates the Bondi radius. The isotropic component of the outward cocoon momentum flux broadly matches the instantaneous (lime) inward Bondi momentum flux at the Bondi radius, tracking the decrease in density at the Bondi radius.

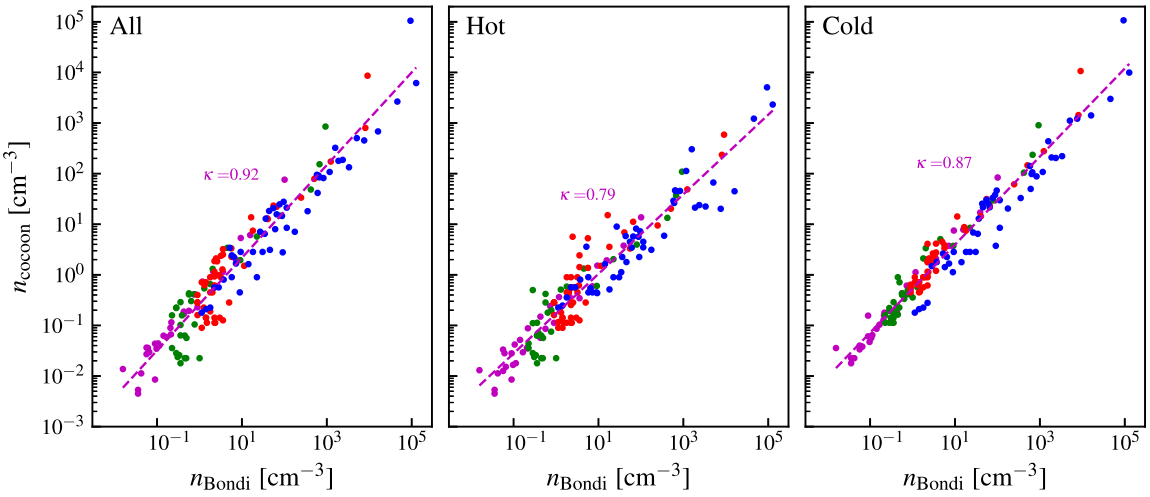

Figure 8. The dependence of the cocoon gas density on background gas properties (evaluated at the Bondi radius) for the 10^4M$_\odot$ run. Each simulation is divided into 0.1 Myr periods, and the average quantities for each period are plotted. The dots of the same colour are from the same simulation. The lines are fitted power laws with the index (κ) labelled. The cocoon is defined for simplicity as all gas with $T > 1.2T_\infty$, and hot gas as gas with $T > 3.6T_\infty$. We find $n_c \propto n_\infty^\zeta T_\infty^\xi$ with $\zeta \lesssim 0.9$.

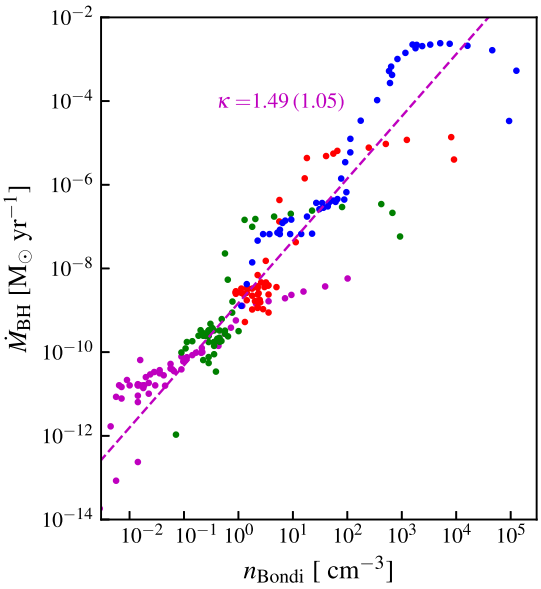

Figure 9. The dependence of the jet mass flux ($\dot{M}_{\rm jet}$) on the background gas properties for $M_{\rm BH} = 10^4$M$_\odot$. The run is divided into 0.8 Myr periods, and the accretion rate and background gas density at the Bondi radius averaged over each specific time period are plotted. Each colour represents one run. The lines show power-law fits, with the index (κ) labelled. The number in parentheses is an estimate from the toy model, and the fit to the cocoon gas-phase dependence in Fig. 8 roughly agrees with what we measured from the simulation.

where

$$\alpha_1 \sim 1.1 \quad \alpha_2 \sim 1.05$$
$$\tau_1 \sim 0.6 \text{ (for } M_{\rm BH} = 1{\rm M}_\odot) \text{ to } -0.2 \text{ (for } M_{\rm BH} = 100\,{\rm M}_\odot)$$
$$\tau_2 \sim -0.2 \text{ (for } M_{\rm BH} = 1{\rm M}_\odot) \text{ to } -0.6 \text{ (for } M_{\rm BH} = 100\,{\rm M}_\odot) \quad (15)$$

Note that from the simulations, we measure $\alpha_1 \sim \alpha_2 \sim 1.5$.

Fig. 10 shows the comparison of the scaling from the toy model to the simulation results. The background colour represents the toy model's predictions, while each circle corresponds to one run, coloured by the actual measured accretion rate from the simulation. The first three rows show the results for 1 M$_\odot$, 100 M$_\odot$, and the first 0.2 Myr of 10^4 M$_\odot$, respectively. For the left panel, which shows the scaling of the accretion rate with gas temperature and density, we assume $r_{\rm iso} > r_{\rm Bondi}$, as it describes most of the parameter space there. All of them show reasonable agreement with the toy model's prediction. We note that for BH masses larger than 100 M$_\odot$, super-Eddington accretion is possible in part of the parameter space with low feedback efficiency, high gas density, and low gas temperature.

For $M_{\rm BH} = 10^4$ M$_\odot$, there is a significant decay in the accretion rate after the initial period, as shown in Fig. 1. We provided an analytical description of how the jet cocoon propagates once density suppression occurs in Section 5.

5 AN ANALYTIC MODEL FOR THE TERMINAL RADIUS OF THE JET COCOON EXPANSION

In this section, we generalize the model previously developed to provide a quantitative understanding of how the jet cocoon evolves once density suppression occurs. From the discussion above, we know the following facts when the density is suppressed:

(i) The isotropic component of the cocoon momentum flux is regulated to the real-time inflowing Bondi momentum flux, given the current density at the Bondi radius. Thus, $\dot{M}_{\rm BH} \propto n_{\rm Bondi}^\alpha$.
(ii) Density suppression occurs beyond $r_{\rm iso}$ when $r_{\rm terminal} > r_{\rm iso}$ and $r_{\rm terminal} > r_{\rm core}$.
(iii) The BH can 'feel' the density suppression if the Bondi radius, $r_{\rm Bondi}$, is larger than $r_{\rm iso}$ but smaller than $r_{\rm terminal}$, as the density at $r_{\rm Bondi}$ will decrease over most of the solid angle. For simplicity, we do not consider density suppression when $r_{\rm Bondi} < r_{\rm core}$.
(iv) Density suppression begins to affect the BH as soon as the jet cocoon propagates through the Bondi radius.
(v) When density suppression occurs, the density within the suppressed region becomes roughly constant at the density of the current position of the cocoon shock front.

The key assumption we will make to derive the location of the terminal radius is that the jet cocoon terminates when the cumulative energy flux of the jet equals the time-integrated cooling rate within

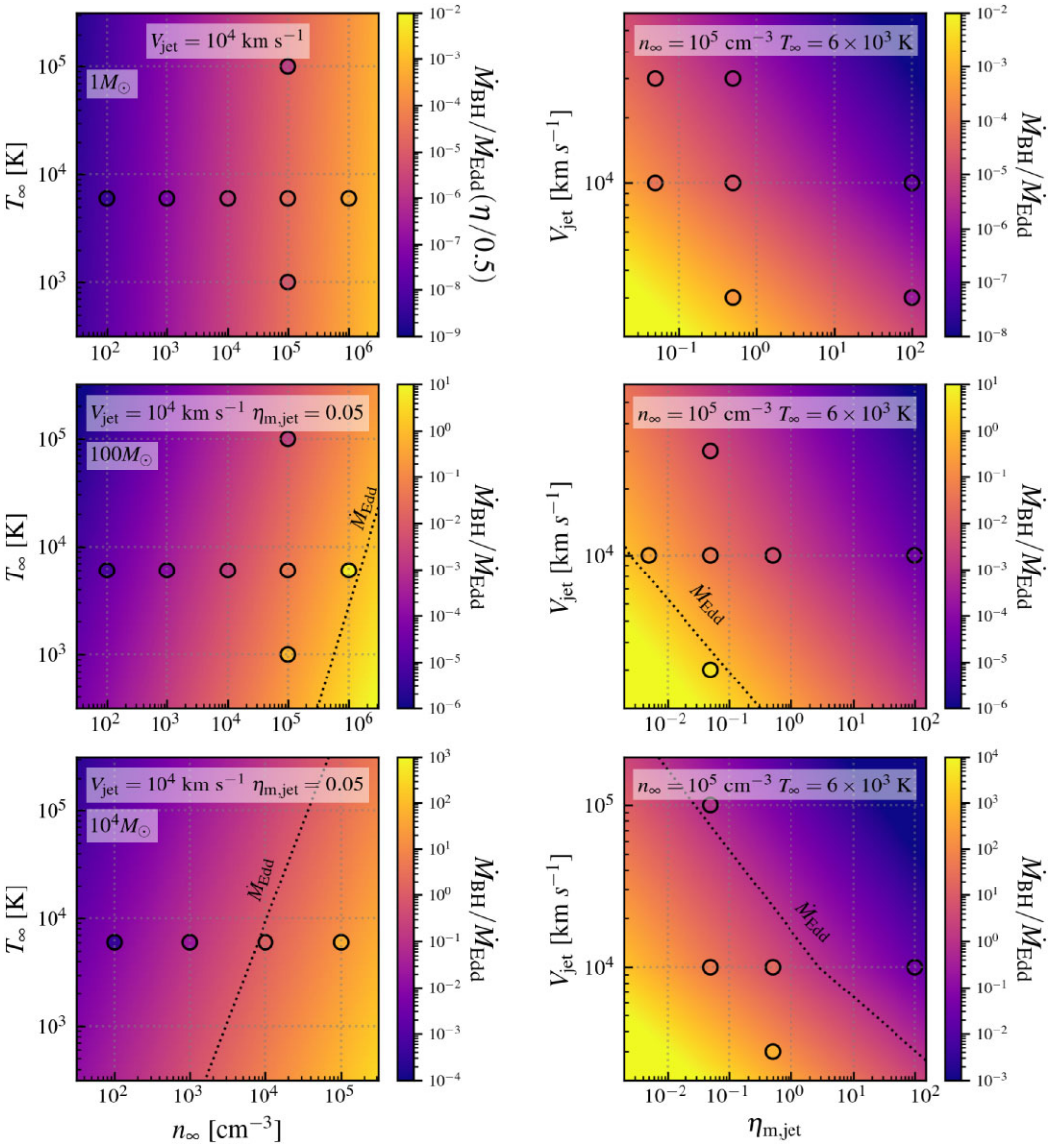

Figure 10. The predicted $\dot{M}_{\rm acc}/\dot{M}_{\rm Edd}$ from the scaling of our toy model, assuming normalization to the fiducial runs, is shown as the background colour in each panel. Runs with low background gas temperature (T_∞), high background gas density (n_∞), low jet velocity ($V_{\rm jet}$), or low feedback mass loading ($\eta_{\rm m,jet}$) result in super-Eddington accretion for cases with $M_{\rm BH} \gtrsim 100\,{\rm M}_\odot$. Black dotted lines indicate Eddington accretion. The results from the simulations are shown as circles, colored with the measured value in order to give an indication of how well the model fares in predicting the simulation results. The three rows show the cases for 1 $\rm M_\odot$, 100 $\rm M_\odot$, and the first 0.2 Myr of 10^4 $\rm M_\odot$. The left column shows the results as a function of gas properties, while the right column shows the results as a function of AGN jet parameters. They show a qualitative agreement with the toy model.

the jet cocoon. Once this occurs, the jet cocoon can no longer propagate, and the influence of the cocoon on the surrounding gas becomes minimal. Equipped with this information, we can write down an analytical description of cocoon propagation. In Section 5.1, we will derive the integrated jet energy flux, in Section 5.2, we will compute the cocoon radiative cooling rate and, in Section 5.3, we will equate these to determine the terminal radius.

5.1 Integrated jet energy flux

Given the points above, we consider density suppression to start the moment ($t = t_{\rm Bondi}$) when an isotropized jet cocoon, with radius $R(t)$, passes through the Bondi radius, which is equal to or larger than the core radius. We will use $\rho_{0,\,\rm Bondi}$ ($n_{0,\,\rm Bondi}$) to denote the initial background gas (number) density at the Bondi radius, $r_{\rm Bondi}$ when $t = t_{\rm Bondi}$. We note that for our runs with an initial BH mass of 10^4 $\rm M_\odot$, this radius is ~ 1 pc, which is also the core radius, $r_{\rm core}$. In that case, the initial number density at the Bondi radius, $n_{0,\,\rm Bondi}$, is also the initial core gas density, $n_{0,\,\rm core}$.

In our previous paper (Su et al. 2023b), we derived the energy conservation equation governing the conversion of jet energy flux into cocoon energy flux during the bubble ($R(r) > r_{\rm iso}$) phase, as well as the momentum conservation at the cocoon shock front for a uniform-density background medium. Given the density evolution within the Bondi radius, the gas density also becomes a function of time.

$$4\pi R(t)^2 \rho_c(t) V_{\rm R,\,Hot}^3(t) = \frac{\gamma}{2}\dot{M}_{\rm jet}(t) V_{\rm jet}^2$$
$$V_{\rm R,\,Hot}^2(t)\rho_c(t) = V_{\rm R}^2(t)\rho(t), \quad (16)$$

where $V_{\rm R,\,Hot}(t)$ and $\rho_c(t)$ are the velocity and density of the hot phase of gas, respectively, while $V_{\rm R}(t)$ is the cocoon propagation velocity, and $\rho(t)$ is the density at the shock front of the jet cocoon.

When $R(t)$ reaches $r_{\rm Bondi}$ at $t = t_{\rm Bondi}$, we define:

$$\rho(t_{\rm Bondi}) = \rho_{0,\,\rm Bondi},\quad \rho_c(t_{\rm Bondi}) = \rho_{0,\,\rm c},\quad \text{and}\quad \dot{M}_{\rm jet}(t_{\rm Bondi}) = \dot{M}_{0,\,\rm jet}. \tag{17}$$

After $R(t)$ reaches $r_{\rm Bondi}$, the gas between $r_{\rm iso}$ and $R(t)$ remains at approximately constant density. Since $r_{\rm Bondi}$ lies within this radial range, $\rho_{\rm Bondi}(t) = \rho(t)$.

Since the density profile follows $\rho(r) \propto n(r) \propto r^{-2}$ in the radial range we are considering, we have

$$\rho_{\rm Bondi}(t) = \rho(t) = \rho_{0,\,\rm Bondi}\left(\frac{R(t)}{r_{0,\,\rm Bondi}}\right)^{-2}$$
$$\rho_{\rm c}(t) = \rho_{0,\,\rm c}\left(\frac{R(t)}{R_{\rm core}}\right)^{-2}. \tag{18}$$

Supposed $\dot{M}_{\rm jet}(t) \propto \rho^{\alpha}_{\rm Bondi}(t) \propto n^{\alpha}_{\rm Bondi}(t)$, we have

$$\dot{M}_{\rm jet}(t) = \dot{M}_{0,\,\rm jet}\left(\frac{\rho(t)}{\rho_{0,\,\rm Bondi}}\right)^{\alpha} = \dot{M}_{0,\,\rm jet}\left(\frac{R(t)}{r_{\rm Bondi}}\right)^{-2\alpha}. \tag{19}$$

Following the toy model summarized in Section 3.1, equation (8) can be generalized as $n_c(t) \propto n^{\xi}_{\rm Bondi}(t)$ with $\xi \lesssim 1$. Equation (11) also gives $\alpha \sim (3-\xi)/2$ for the isotropic case.

Putting equations (16), (18), and (19) together, we get:

$$V_R(R) = \left(\frac{\gamma}{8\pi}\right)^{1/3} \dot{M}^{1/3}_{0,\,\rm jet} V^{2/3}_{\rm jet} \rho^{1/6}_{0,\,c} \rho^{-1/2}_{0,\,\rm Bondi} r_{\rm Bondi}^{\frac{-2+2\alpha}{3}} R^{-2\alpha/3}(t), \tag{20}$$

and

$$R(t) = \left[\left(\frac{2\alpha+3}{3}\right)^3 \frac{\gamma}{8\pi}\right]^{\frac{1}{3+2\alpha}} \dot{M}^{\frac{1}{3+2\alpha}}_{0,\,\rm jet} V^{\frac{2}{3+2\alpha}}_{\rm jet} \rho^{\frac{1}{6+4\alpha}}_{0,\,c} \rho^{\frac{-3}{6+4\alpha}}_{0,\,\rm Bondi} r_{\rm Bondi}^{\frac{-2+2\alpha}{3+2\alpha}} t^{\frac{3}{2\alpha+3}}. \tag{21}$$

The net integrated energy flux from the time when $R(t_{\rm Bondi}) = r_{\rm Bondi}$ is

$$\begin{aligned} E_{\rm tot,\,jet}(t) &= \int \frac{1}{2}\dot{M}_{\rm jet} V^2_{\rm jet} {\rm d}t \\ &= \int_{t_{\rm Bondi}}^{t} \frac{1}{2}\dot{M}_{0,\,\rm jet}\left(\frac{R(t)}{R_{\rm Bondi}}\right)^{-2\alpha} V^2_{\rm jet} {\rm d}t \\ &= \frac{1}{2}\left[\left(\frac{2\alpha+3}{3}\right)^3 \frac{\gamma}{8\pi}\right]^{\frac{-2\alpha}{3+2\alpha}} \dot{M}^{\frac{3}{3+2\alpha}}_{0,\,\rm jet} V^{\frac{6}{3+2\alpha}}_{\rm jet} \rho^{\frac{-2\alpha}{6+4\alpha}}_{0,\,\rm c} \rho^{\frac{6\alpha}{6+4\alpha}}_{0,\,\rm Bondi} \\ &\quad r_{\rm Bondi}^{\frac{10\alpha}{3+2\alpha}} \left[\frac{2\alpha+3}{4\alpha-3}\left(t_{\rm Bondi}^{\frac{3-4\alpha}{2\alpha+3}} - t^{\frac{3-4\alpha}{2\alpha+3}}\right)\right], \end{aligned} \tag{22}$$

or in terms of the position of the shock front,

$$\begin{aligned} E_{\rm tot,J}(R) &= \int \frac{1}{2}\dot{M}_{\rm jet} V^2_{\rm jet} {\rm d}t \\ &= \int_{r_{\rm Bondi}}^{R} \frac{1}{2}\dot{M}_{0,\,\rm jet}\left(\frac{R}{r_{\rm Bondi}}\right)^{-2\alpha} V^2_{\rm jet} V_R^{-1}(R) {\rm d}R \\ &= \left(\frac{\gamma}{\pi}\right)^{-1/3} \dot{M}^{2/3}_{0,\,\rm jet} r_{\rm Bondi}^{\frac{2+4\alpha}{3}} V^{4/3}_{\rm jet} \rho^{1/6}_{0,\,\rm c} \rho^{1/2}_{0,\,\rm Bondi} \\ &\quad \left(\frac{3}{4\alpha-3}\right)\left(r_{\rm Bondi}^{\frac{3-4\alpha}{3}} - R^{\frac{3-4\alpha}{3}}\right). \end{aligned} \tag{23}$$

This saturates to a maximum value:

$$\begin{aligned} E_{\rm max,\,jet} &= \left(\frac{\gamma}{\pi}\right)^{-1/3} \dot{M}^{2/3}_{0,\,\rm jet} r^{\frac{5}{3}}_{\rm Bondi} V^{4/3}_{\rm jet} \rho^{-1/6}_{0,\,\rm c} \rho^{1/2}_{0,\,\rm Bondi} \left(\frac{3}{4\alpha-3}\right) \\ &\propto n^{\frac{2\alpha}{3}-\frac{\xi}{6}+\frac{1}{2}}_{0,\,\rm Bondi}. \end{aligned} \tag{24}$$

From Figs 8 and 9, where we measured $\xi = 0.9$ and $\alpha = 1.5$, we obtain $E_{\rm max,\,jet} \propto n^{1.35}_{0,\,\rm Bondi}$.[3]

5.2 The integrated cocoon cooling

The instantaneous cooling rate within the jet cocoon at a specific time after $R(t_{\rm Bondi}) = r_{\rm Bondi}$ is given by:

$$\begin{aligned} \dot{E}_{\rm cool}(R) &= \int_0^R \frac{d\dot{E}_{\rm cool}}{d\,{\rm Vol}} 4\pi r^2 {\rm d}r \\ &= \int_0^R \Lambda 4\pi n_{\rm c,\,e}(R) n_{\rm c,\,H}(R) r^2 {\rm d}r \\ &\sim \Lambda \frac{4\pi}{3} n_{\rm c,\,e}(R) n_{\rm c,\,H}(R) R^3 \\ &\sim \Lambda' \frac{4\pi}{3} n^2_{0,\,\rm c}\left(\frac{R}{r_{\rm Bondi}}\right)^{-4} R^3, \end{aligned} \tag{25}$$

where Λ is the cooling function, and $n_{\rm c,\,e}(R)$ and $n_{\rm c,\,H}(R)$ denote the electron and hydrogen number densities of the jet cocoon gas, respectively. Given the assumption of constant density within the jet cocoon, both are constant with respect to r but scale with R, the current position of the cocoon shock front, following equation (18). Λ' accounts for the conversion from hydrogen or electron number density to the overall gas cocoon number density. To estimate the cooling function, the cocoon gas is mostly from $10^5 - 10^8$ K, for which $\Lambda \sim 10^{-23}{\rm erg\,s^{-1}cm^3}$.

The accumulated cooling up $R(t_{\rm Bondi}) = r_{\rm Bondi}$ to the time the bubble reaches R would then be:

$$\begin{aligned} E_{\rm cool}(R) &= \int \dot{E}_{\rm cool}(t) {\rm d}t \\ &= \int_{r_{\rm Bondi}}^{R} \dot{E}_{\rm cool}(R) V_R^{-1}(R) {\rm d}R \\ &= \frac{4\pi}{3}\Lambda' n^2_{0,\,\rm c} r_{\rm Bondi}^{\frac{-2\alpha+14}{3}} \left(\frac{\gamma}{8\pi}\right)^{-1/3} \dot{M}^{-1/3}_{0,\,\rm jet} \\ &\quad V^{-2/3}_{\rm jet} \rho^{-1/6}_{0,\,\rm c} \rho^{1/2}_{0,\,\rm Bondi} \left(\frac{3}{2\alpha}\right)\left(R^{\frac{2\alpha}{3}} - r_{\rm Bondi}^{\frac{2\alpha}{3}}\right) \\ &\propto n^{11/6}_{0,\,\rm c} n^{1/2-\alpha/3}_{0,\,\rm Bondi} R^{\frac{2\alpha}{3}} \qquad (\text{for } R >> r_{\rm Bondi}) \end{aligned} \tag{26}$$

5.3 The terminal radius

Finally, we derive the terminal radius by balancing heating and cooling, or in other words setting $\dot{E}_{\rm cool}(R) \sim \dot{E}_{\rm max,\,jet}(R)$ and solving for $R = r$terminal. For $\alpha = 1.5$ and $\xi = 0.9$, we have

$$r_{\rm terminal} \sim 12\,{\rm pc}\left(\frac{n_{0,\,\rm Bondi}}{10^3\,{\rm cm^{-3}}}\right)^{0.3} \sim 12\,{\rm pc}\left(\frac{n_{0,\,\rm core}}{10^3\,{\rm cm^{-3}}}\right)^{0.3}. \tag{27}$$

We find a very weak dependence on the gas density, which is roughly comparable to the value shown in Fig. 5.

[3]Alternatively, if we only use $\xi = 0.9$ from Fig. 8 and substitute it into equation (11) to get $\alpha = 1.05$, we find $E_{\rm max,\,jet} \propto n^{1.05}_{0,\,\rm Bondi}$.

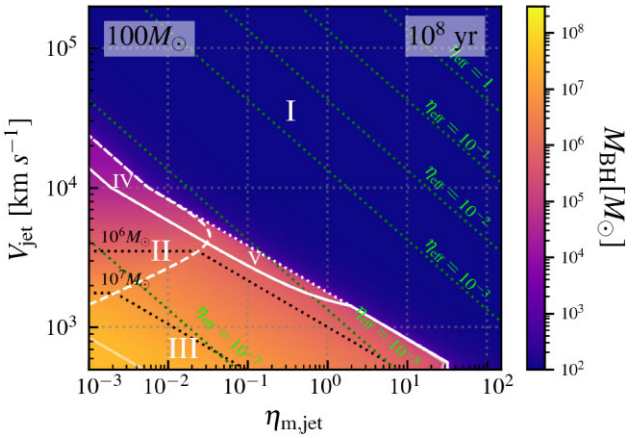

Figure 11. The prediction of the black hole mass 100 Myr after seeding a 100 $M_\odot$ black hole in our fiducial profile of an atomic-cooling halo is as follows: black holes with high-efficiency feedback (I, above the dotted line) never grow out of the constant-density phase. Black holes with low-efficiency feedback (II and III, below the solid white line) undergo an extended 'fail to regulate' phase, where most of the mass is accreted. If the feedback efficiency is very low (below the light white line), the black hole has not re-entered the self-regulation phase at the time. Black holes with intermediate-efficiency feedback (IV and V, between the dashed and solid white lines) never go through a 'fail to regulate' phase. Black holes with feedback parameters to the left of the dashed line (II and IV) end up going through a core density suppression phase. The maximum efficiency allowed for forming a supermassive black hole with $M_{\rm BH} > 10^6 M_\odot$ is $\eta_{\rm eff} = 10^{-5}$. See Section 6.1 for discussion.

6 PUTTING IT ALL TOGETHER: PREDICTING SEED BLACK HOLE GROWTH FOR AN ATOMIC-COOLING HALO

In this section, we combine the analytic model we have developed with the expected conditions for atomic-cooling haloes to determine how much BH growth we expect under various conditions. In Section 6.1, we discuss the detailed calculations behind this plot and the different phases of growth. In Section 6.2, we explore how these results change with BH seed mass and time, and in Section 6.3, we highlight the importance of the feedback efficiency. We first review the contents of our analytic understanding, which includes:

(i) How a jet cocoon propagates in a constant density environment (Section 3.1).
(ii) How a jet cocoon propagates in an $n \propto r^{-2}$ environment undergoing density suppression (Section 5).
(iii) How BH accretion is regulated by jets in a constant density environment (Section 3.2).
(iv) How BH accretion is regulated by jets in an $n \propto r^{-2}$ decay environment undergoing density suppression (Section 5.3).

Equipped with this knowledge, we can predict the growth of a BH seeded in the fiducial density profile, with $n = 10^5\,{\rm cm}^{-3}$ within $r_{\rm core} = 1$ pc and an $n \propto r^{-2}$ profile outside of that, typical of high-redshift ($z \sim 20$) atomic-cooling haloes (e.g. Regan et al. 2019).

For a seed BH mass of 100 $M_\odot$ (an expected outcome of first star formation), the predicted BH mass after 10^8 yr as a function of the AGN feedback parameter is shown in Fig. 11. As we will describe in more detail below, we find the growth depends principally on the effective jet energy efficiency ($\eta_{\rm eff}$). After 10^8 yr, a BH can possibly grow to $10^6\,M_\odot$ when $\eta_{\rm eff} < 10^{-5}$ and to $10^7\,M_\odot$ when $\eta_{\rm eff} < 10^{-7}$. The lower the feedback mass loading and the lower the jet velocity, the faster the BH will grow. The transition is sharp; if $\eta_{\rm eff} < 10^{-4}$, the BH grows beyond its initial mass.

6.1 The phases of growth

To determine the overall amount of mass a BH can accrete, accounting for the jet feedback detailed in this paper, we first need to determine the phases that the system passes through, which we can broadly classify into two cases:

(i) **BH growth with $r_{\rm Bondi} < r_{\rm core}$ (constant density)**: for jet-based self-regulation in this case, the accretion rate is described by equations (14) and (15), but note that $\dot{M}_{\rm BH} + \dot{M}_{\rm jet}$ should be capped by $\dot{M}_{\rm Bondi}$. If the required $\dot{M}_{\rm jet}$ in equations (14) and (15) is higher than this value, $\dot{M}_{\rm BH}$ will be at most $\dot{M}_{\rm Bondi}/(1+\eta_{m,fb})$. In both cases, given that the density at the Bondi radius is kept constant in this phase of growth,

$$\dot{M}_{\rm BH} \propto \dot{M}_{\rm Bondi} \propto M_{\rm BH}^2. \tag{28}$$

(ii) **BH growth with $r_{\rm Bondi} > r_{\rm core}$**: when the Bondi radius exceeds the core radius, there are three possibilities:

(a) **Self-regulation without density suppression**: in the case of self-regulation, the accretion rate is still described by equation (11), but with ρ_∞ replaced by $\rho_{\rm Bondi}(t)$. If density suppression does not occur, $\rho_{\rm Bondi}(r_{\rm Bondi})$ is exactly the initial density at the location. As $\rho_{\rm Bondi}(r_{\rm Bondi}) \propto r_{\rm Bondi}^{-2} \propto M_{\rm BH}^{-2}$, we get

$$\dot{M}_{\rm BH} \propto M_{\rm BH}^2 \rho^\alpha \propto M_{\rm BH}^{-1}, \tag{29}$$

where we follow equation (14) but adopted $\alpha \sim 1.5$, as seen in the simulations.

(b) **Failure to regulate**: if the required $\dot{M}_{\rm jet}$ in equations (14) and (15) implies that $\dot{M}_{\rm jet} + \dot{M}_{\rm BH}$ is higher than $\dot{M}_{\rm Bondi}$, then, as before, $\dot{M}_{\rm BH}$ will be at most $\dot{M}_{\rm Bondi}/(1+\eta_{m,fb})$. In such a case,

$$\dot{M}_{\rm BH} \propto \dot{M}_{\rm Bondi} \propto M_{\rm BH}^2 \rho \propto \text{constant}, \tag{30}$$

so that the accretion rate is independent of $M_{\rm BH}$.

(c) **Self-regulation with density suppression**: finally, density suppression occurs when $r_{\rm Bondi} > r_{\rm core}$ and $r_{\rm Bondi} > r_{\rm iso}$. After density suppression, the jet energy flux evolution follows equation (23) as $\dot{M}_{\rm BH} = 2\dot{E}_{\rm tot,J}/(\eta_{\rm m,fb} V_j^2)$, which barely grows due to the rapid density drop as the cocoon propagates. Note that in this phase, realistically, the propagation of the shock front stops at the terminal radius. After that, another episode of accretion can occur, and we could calculate it by adopting an effective profile with a core radius at the first $r_{\rm terminal}$ and the original density at $r_{\rm terminal}$ as the core density. However, due to the large suppression of the core density, this will not result in significant accretion, and so we neglect such a second or subsequent episode of accretion in Fig. 11 (and Fig. 12, which will be discussed in Section 6.2).

To help guide understanding of these phases and how they connect to the calculated BH growth, we use Roman numerals in Fig. 11 (and Fig. 12) to represent different growth histories, as indicated below. Each Zone indicates the different sequence of growth histories using the notation of the previous enumeration, indicated by arrows.[4] To visualize the sequences described above, Fig. 13 presents typical

[4]So, for example Zone II begins with constant density accretion until the BH mass grows such that its Bondi radius reaches the halo core radius,

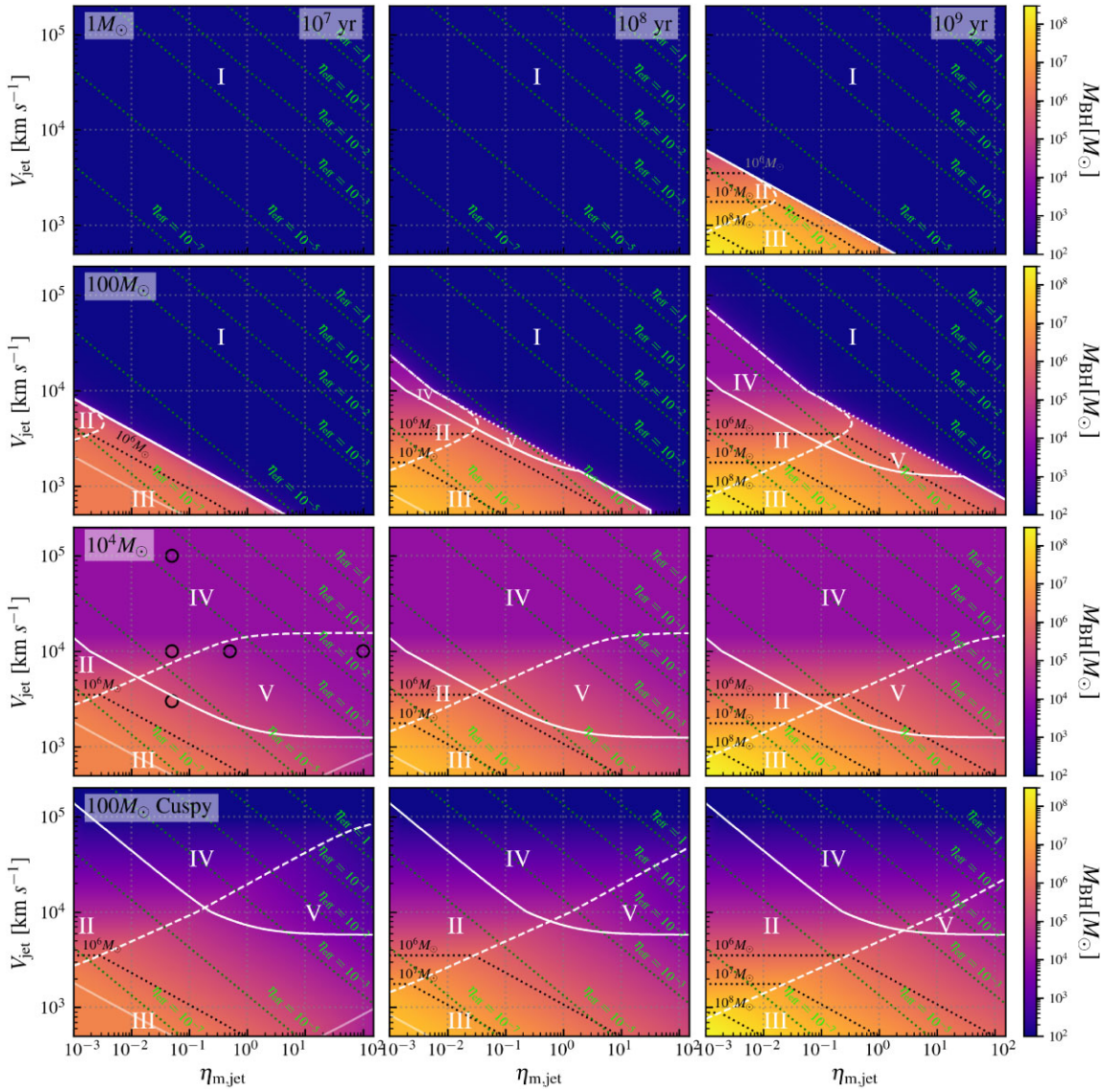

Figure 12. The prediction of the black hole mass at 10^7 (left column), 10^8 (centre column), and 10^9 yr (right column) after seeding a 1 (first row), 100 (second row), and 10^4 $M_\odot$ (third row) black hole in our fiducial profile of an atomic-cooling halo. The fourth row shows the results for seeding a 100 $M_\odot$ black hole, assuming a more cuspy profile with $n_{\rm core} = 10^9$ cm^{-3} and core radius $r_{\rm core} = 10^{-2}$ pc. Green dotted lines indicate constant jet energy efficiency, while white lines delineate accretion regions and are described in the text. Seeding a more massive black hole or assuming a cuspy profile of the atomic-cooling halo only affects the final mass for black holes with higher efficiency feedback.

examples of BH growth with different feedback parameters, each falling into distinct zones. The phases of BH growth in each zone are represented by different line styles, with phase transitions indicated by dots.

(i) Zone I: the BHs here have high-efficiency feedback, so they never grow beyond 10^4 $M_\odot$.

at which point it undergoes an episode of rapid growth due to failed self-regulation until the Bondi radius reaches a sufficiently low density (since $\rho \propto r^{-2}$) that regulation can be re-established, but without driving density suppression in the core (and, if there is sufficient time, the Bondi radius will grow while the isotropization radius shrinks. Once the Bondi radius exceeds the isotropization radius, the BH will 'fee' density suppression).

(i) BH growth in constant density

(ii) Zone II: the BH here has low-efficiency feedback and goes through the fail-to-regulate phase. The isotropization radius is also small enough that, eventually, density suppression occurs.

(i) BH growth in constant density ⇒ (ii-b) Fail to regulate ⇒ (ii-c) Self-regulation w/o density suppression ⇒ (ii-a) Self-regulation with density suppression

(iii) Zone III: the BH here has low-efficiency feedback and goes through the fail-to-regulate phase. The isotropization radius is large enough that density suppression has not occurred.

(i) BH growth in constant density ⇒ (ii-b) Fail to regulate ⇒ (ii-c) Self-regulation w/o density suppression

(iv) Zone IV: the BH here has intermediate-efficiency feedback and never fails to regulate. The isotropization radius is also small enough that, eventually, density suppression occurs.

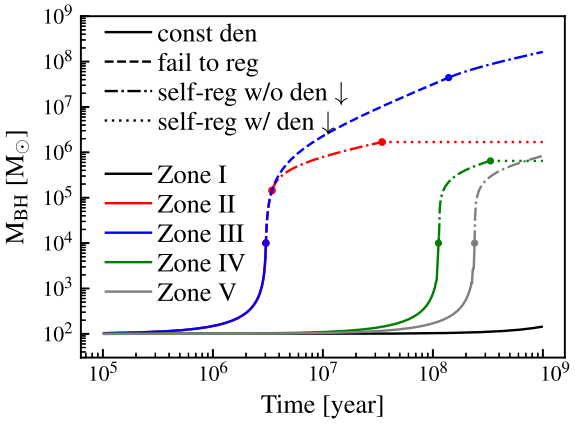

Figure 13. Examples of black hole growth with different feedback parameters ($\eta_{\rm m,fb}$, $V_{\rm jet}$) fall into distinct zones: Zone I ($0.02, 3\times10^4\,{\rm km\,s^{-1}}$), Zone II ($0.005, 3\times10^3\,{\rm km\,s^{-1}}$), Zone III ($0.002, 6\times10^2\,{\rm km\,s^{-1}}$), Zone IV ($0.1, 4\times10^3\,{\rm km\,s^{-1}}$), and Zone V ($0.5, 3\times10^3\,{\rm km\,s^{-1}}$). The phases of black hole growth that each zone undergoes (see Section 6.1) are represented by different line styles, with the phase transitions marked by dots.

(i) BH growth in constant density ⇒ (ii-c) Self-regulation w/o density suppression ⇒ (ii-a) Self-regulation with density suppression

(v) Zone V: the BH here has intermediate-efficiency feedback and never fails to regulate.The isotropization radius is large enough that density suppression has not occurred.

(i) BH growth in constant density ⇒ (ii-c) Self-regulation w/o density suppression

Note that for cases with $10^4\,M_\odot$ (and $100\,M_\odot$ with a cuspy profile), the initial Bondi radius coincides with the core radius, so the BH has never been through phase (i), and hence there is also no Zone I, as shown in Fig. 12. We will discuss this in Section 6.2. BHs with low feedback efficiency (below the light white line in Figs 11 and 12) have not re-entered the self-regulation phase at the corresponding time.

6.2 Dependence on seed black hole mass and time

Fig. 12 shows 12 cases with different seed BH masses ($1\,M_\odot$, $100\,M_\odot$, $10^4\,M_\odot$), and predictions after 10^7, 10^8, and 10^9 yr, and within each panel, the result is shown as a function of jet parameters. The fourth row shows a case with a $100\,M_\odot$ initial BH, but assuming a more cuspy profile, with $n_{\rm core}=10^9\,{\rm cm^{-3}}$ and core radius $r_{\rm core}=10^{-2}$ pc. In the cases with $10^4M_\odot$ and $100\,M_\odot$ in cuspy profiles, the Bondi radius starts at the core radius, so they do not go through growth in the constant density profile [phase (i)].

For the $10^4M_\odot$ case, we have run some simulations to $\sim10^7$ yr, allowing an exact comparison with our toy model. The simulation results are marked with circles in the corresponding panel (third row, 1st column). The colours in the circles indicate the BH mass at the end of the simulation, which agrees extremely well with the prediction based on the toy model.

Taking the $100\,M_\odot$ case as an example, at 10^7 yr, the majority of the parameter space is still in the constant density phase and has not grown much from its initial mass. Only the lowest efficiency cases grow beyond $10^4M_\odot$, mostly due to the 'fail to regulate' phase. As time evolves, the intermediate efficiency region grows out of the constant density phase and starts to grow, leading to regions IV and V. As time progresses, more of the parameter space grows out of the constant density phase, and regions IV and V become larger.

The parameter space with efficiency lower than the light white line between IV/V and II/III (Zone II, III) undergoes a 'fail to regulate' phase. As the BH grows, the Bondi radius increases, and the density at the Bondi radius decreases. However, the required mass flux for regulation scales with $\rho^{1.5}$, while the Bondi accretion rate scales with n. As the density decays, self-regulation eventually resumes.

For the highest efficiency parameter space (I), the BH never grows much beyond its initial mass. For the intermediate efficiency parameter space (IV, V), the BH never fails to regulate. For the parameter space to the left of the dashed white line, the BH undergoes a phase of suppressing the density halo due to jet cocoon propagation.

Changing the seed BH mass mostly affects the high-efficiency part of the parameter space. BHs with high-efficiency feedback grow very slowly, so having a head start with a higher seed mass significantly increases the resulting BH mass. For the cases with lower efficiency, which do grow to SMBHs, changing the seed mass does not change the result, as they reach a BH mass much larger than $10^4\,M_\odot$ within a very short time period anyway. The exceptions are the $1\,M_\odot$ cases within 10^8 yr. Decreasing the seed BH mass to that level prevents any of the cases from growing beyond $100\,M_\odot$ within the designated time.

Having a cuspy profile also helps the initial BH growth (bottom panel). However, BHs with feedback in the low-efficiency parameter space grow to large masses very quickly regardless, so the cuspy profile hardly matters.

We note that, realistically, the final BH mass for seeding $100\,M_\odot$ BHs in a cuspy profile should be strictly larger than seeding them in a fiducial profile. We see this is not the case for the upper left corner. This artefact is mostly due to the simplification in the theoretical calculation caused by not considering the core density suppression before the BH grows to $10^4\,M_\odot$ when $r_{\rm Bondi}$ reaches $r_{\rm core}=1$ pc. Realistically, such suppression can happen earlier when the cocoon isotropizes, and the shock front already propagates beyond $r_{\rm core}$. Therefore, we slightly overestimate the final BH mass for the upper left corner of region IV for the $100\,M_\odot$ fiducial profile case.

6.3 Maximum feedback efficiency for forming supermassive black hole

Fig. 14 shows the maximum jet efficiency ($\eta_{\rm eff}$ defined in equation 4) that will allow a BH to grow to intermediate mass scale ($10^4-10^6M_\odot$; top panel) or SMBHs ($>10^6M_\odot$; top panel) as a function of time, for different seed masses and halo properties (assuming $V_{\rm Jet}>500\,{\rm km\,s^{-1}}$). For most cases, except for the $1\,M_\odot$ seed, an efficiency smaller than $\eta_{\rm eff}=(10^{-6},10^{-5},10^{-4})$ is required for the BH to grow to supermassive size within $t=(10^7,10^8,10^9)$ yr.

Seeding a $1\,M_\odot$ BH requires more than 2 orders of magnitude lower efficiency to grow to supermassive size within the same time frame, and it is only possible after 3×10^8 yr. Having a cuspy profile or seeding a $10^4\,M_\odot$ BH slightly increases the efficiency upper bound for SMBHs, by a similar extent, within a factor of 2.

However, having cuspier density profiles and increasing the seed BH mass can increase the allowed feedback efficiency for forming IMBHs by orders of magnitude. Both of these factors give the BH growth a head start, allowing BHs with feedback over a larger parameter space to grow to $>10^4\,M_\odot$.

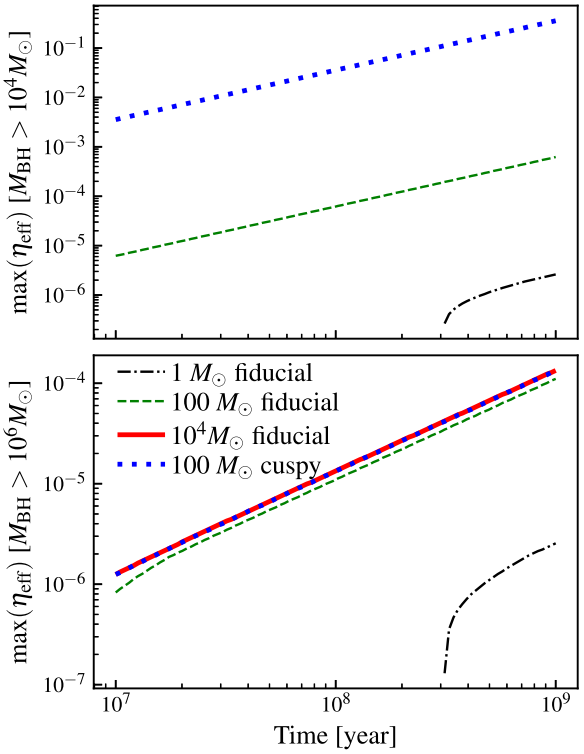

Figure 14. The maximum efficiency for seeding different halo masses in different gas profiles, allowing the black hole to grow to intermediate mass black holes ($10^4 - 10^6\,M_\odot$, upper) or supermassive black holes ($> 10^6\,M_\odot$, lower) assuming $V_{\rm Jet} > 500\,{\rm km\,s^{-1}}$, is shown as a function of time. For most cases, except for a $1\,M_\odot$ seed, an efficiency smaller than $\eta_{\rm eff} = (10^{-6}, 10^{-5}, 10^{-4})$ is required for the black hole to grow to supermassive status by $t = (10^7, 10^8, 10^9)$ yr. Having cuspier density profiles and increasing the seed black hole mass can increase the feedback efficiency upper bound for forming intermediate mass black holes by orders of magnitude.

7 DISCUSSION

7.1 The choice of seed masses and gas profiles

In this work, we surveyed a full BH seed mass range of $1 - 10^4\,M_\odot$. We note that BH masses are typically much larger than $1\,M_\odot$, and BH remnants of Population III stars may be heavier than $100\,M_\odot$ (Bromm, Coppi & Larson 1999, 2002; Abel, Bryan & Norman 2002). The inclusion of $1\,M_\odot$ in this study is primarily for testing the applicability of the analytical model over a wide range in BH mass. We also note that $10^4\,M_\odot$ represents the lower end of the BH mass range for direct collapse BHs and emphasize the importance of investigating more massive cases for future work.

The fiducial gas density profile was motivated by a typical atomic cooling halo, as described in, for example Regan et al. (2019). We varied the slope of the density profile around the fiducial value. However, since our study tests BH accretion within a single typical atomic cooling halo scenario across different seed masses, we did not modify the density profile range when varying the BH seed mass. The fiducial profile essentially sets the range of T_∞ and n_∞ (or $T_{\rm Bondi}$ and $n_{\rm Bondi}$) in the simulations. We note that we expect – and did recover – a Bondi-like solution, $n \propto r^{-3/2}$, after the run starts, in the absence of feedback, which should represent the steepest slope possible without incorporating additional physics, such as net angular momentum.

7.2 Limitations of the model

In this work, we focus on set-ups with constant initial temperature and an idealized density profile: a core with constant density within 1 pc, transitioning to an $n \propto r^{-2}$ profile beyond that. We neglect any initial gas motion, such as turbulence or rotation. While turbulence arises after the jet is launched, we do not include any other causes of gas motion. Realistically, both rotation and turbulence can significantly hinder accretion. We also neglect the presence of magnetic fields, which may further suppress accretion. We emphasize that, while we believe the excluded processes may further suppress accretion, we cannot rule out the possibility that non-linear interactions could produce the opposite effect. For example Schleicher et al. (2009), Sethi, Haiman & Pandey (2010), Turk et al. (2012), and Guo et al. (2024) found that magnetic fields could enhance accretion, whereas Cho et al. (2023, 2024) suggest that magnetic fields might suppress it. These contrasting conclusions likely arise from the distinct gas phases and environmental conditions modelled around the BH in each study. A detailed investigation of these additional physical processes is beyond the scope of this work and will be explored in future studies.

In our simulations, the outer edge of the accretion disc is only marginally resolved during periods of strong accretion. However, since the initial conditions assume no net angular momentum, a transient, rotationally supported structure stochastically forms with random orientation. We, therefore, utilize a sub-grid α-disc model, whose validity can depend significantly on the accretion rate. In our simulations, the Eddington ratio varies widely across runs due to the influence of feedback parameters and shows substantial variability within certain individual runs. For simplicity, we apply the same α-disc model across all runs. Realistically, incorporating such a model primarily affects the short-term variability of accretion rates. As demonstrated in Su et al. (2023b), the long-term averaged behaviour remains largely unaffected, so we do not anticipate significant differences from adopting a more sophisticated accretion disc model. A more detailed study of accretion disc formation and the implementation of a more sophisticated sub-resolution accretion disc model are left for future work.

Our simulations are run for a finite amount of time, capturing only a glimpse of the various phases of BH growth. Although our predictions for BH mass after a time longer than the simulation run-time are based on physical understanding and a toy model that faithfully describes the simulation results, there is a significant extrapolation that needs verification in future work.

We focus solely on jets, which are highly collimated mechanical feedback mechanisms. Realistically, there can be other forms of AGN feedback, such as winds with broader opening angles and radiative feedback, which can result in very different cocoon propagation. We treated the jet velocity and feedback mass loading as constant and free parameters. In reality, these quantities are likely functions of factors such as the accretion rate, BH spin, and accretion disc properties. While our analytical modelling framework remains applicable for more sophisticated feedback models, implementing and testing such models is beyond the scope of this work and will be addressed in future studies.

Most importantly, we neglect other galactic processes like star formation and stellar feedback, which can further suppress BH accretion. We also do not consider the later growth of the atomic-cooling halo or mergers. As a result, our predicted BH mass should be viewed as an upper bound for BHs accreting within a single atomic halo. We emphasize that there are many other channels through which BHs can grow, and we are not able to constrain those in this work.

We also anchor the BH at the centre of the atomic-cooling halo. In reality, the BH seed may 'wander' away from the halo centre and may not be located in the densest region (Regan & Volonteri 2024).

7.3 Observational implication

Despite the limitations discussed in Section 7.2, this work provides a strong constraint on the channel of BH growth that relies on accreting gas within a single atomic-cooling halo. Recent observations with *JWST* have identified a population of SMBHs at relatively high redshifts, beyond $z \sim 6$ and even beyond $z \sim 10$ (e.g. Carnall et al. 2023; Harikane et al. 2023; Kocevski et al. 2023; Larson et al. 2023; Onoue et al. 2023; Übler et al. 2023; Maiolino et al. 2024; Scoggins & Haiman 2024). Assuming an atomic-cooling halo forms at $z \sim 12$ and a BH is seeded immediately, 10^8 and 10^9 yr later would correspond to $z \sim 10$ and $z \sim 5$, respectively.

As shown in Figs 12 and 14, even a small amount of collimated mechanical feedback with relatively low efficiency can significantly hinder BH growth. If we rely on this channel to explain the SMBHs observed by *JWST*, the feedback efficiency should be $\ll 10^{-4}$, and even lower to form those at $z > 10$. Heavy seeds do not help in this scenario, as most of the time spent reaching SMBH status occurs when the BH mass exceeds $10^4\,M_\odot$. Alternatively, the BHs observed at high redshift could form in even denser environments than a typical atomic-cooling halo or grow via other channels.

8 CONCLUSION

In this work, we have utilized a set of idealized simulations with BHs of different masses seeded in various gas environments mimicking the centres of atomic-cooling haloes. Based on these simulations, we provide a toy model describing the propagation of jet cocoons and their resulting regulation of BH growth. Using this toy model, we predict BH mass as a function of time, assuming different seed masses. We found that even with relatively low feedback efficiency, the central density profile of the atomic-cooling halo can be largely suppressed after the first episode of jet cocoon propagation. After this density suppression, BH growth essentially stops. Thus, very low mechanical feedback efficiency is required to form an SMBH at high redshift if relying on feeding a BH by a single atomic-cooling halo. We summarize our conclusions as follows:

(i) We confirm the toy model presented in Su et al. (2023b) for jet cocoon propagation across various BH masses. The propagation of the jet cocoon in the jet direction is governed by momentum conservation, while the lateral expansion is governed by energy conservation due to the pressure in the cocoon. Eventually, the lateral velocity increases and becomes comparable to the velocity in the jet direction at the isotropization radius ($r_{\rm iso}$). Beyond this radius, the jet cocoon becomes an energy-driven isotropic bubble. Lower jet velocity and higher density result in a larger isotropization radius.

(ii) We confirm that despite different comparisons of the isotropization radius ($r_{\rm iso}$) and the Bondi radius ($r_{\rm Bondi}$), it is always the isotropic component of the cocoon momentum that is regulated by the inflowing momentum flux, assuming a Bondi solution at the Bondi radius.

(iii) Super-Eddington accretion can occur when the BH mass reaches approximately $\sim 100\,M_\odot$ in cases with high density, low temperature, and/or low feedback efficiency.

(iv) As the jet cocoon isotropizes and propagates beyond the core radius ($r_{\rm core}$), it can significantly suppress the density profile at the centre of the atomic-cooling halo. This density suppression occurs from the isotropization radius ($r_{\rm iso}$) to the current location of the cocoon shock front, making the density roughly constant within that range. If the Bondi radius ($r_{\rm Bondi}$) falls within this radial range, the BH accretion is affected by the density suppression.

(v) The cocoon will propagate to the terminal radius, where the integrated cooling of the gas within the jet cocoon balances the integrated jet energy flux, stalling its growth.

(vi) Despite the density suppression, we find that the isotropic component of the outflowing momentum flux is still regulated to match the Bondi inflowing momentum at the Bondi radius, accounting for the real-time density at that radius. This results in a secularly evolving regulation scenario.

(vii) Based on an analytic model inspired and calibrated by the simulations, we provide a prediction of BH mass growth as a function of time and BH seed mass, assuming accretion from a single atomic-cooling halo. To form a SMBH within 10^8 and 10^9 yr, we require a jet efficiency of $\eta < 10^{-5}$ and $\eta < 10^{-4}$, respectively.

(viii) For BHs with feedback in the parameter space that allows growth to a SMBH, most of the time is spent when the BH mass exceeds $10^4\,M_\odot$. Therefore, having a heavier seed (at least up to $10^4\,M_\odot$, which represents the lower-mass end of direct collapse BHs) or assuming a cuspier profile does not significantly increase the efficiency upper bound for SMBH formation.

(ix) On the other hand, having a heavier seed or a cuspier profile provides a head start for BH growth, assuming high feedback efficiency. This allows BHs with a larger feedback parameter space to reach IMBHs.

(x) We identified several phases of BH growth (Figs 11 and 12). For the feedback parameter space that allows the formation of SMBHs, most of the accreted mass occurs during the growth phase, where the very low efficiency feedback fails to regulate the Bondi accretion.

We reemphasize that the above conclusions only apply to BH growth relying on feeding within a single typical atomic halo, providing constraints specific to this growth channel. We also neglect stellar physics and magnetic fields, which may further hinder BH growth. Our predictions should be viewed as an upper bound for BH accretion. We leave these other aspects for future study.

ACKNOWLEDGEMENTS

We sincerely thank the anonymous referee for their valuable comments and suggestions, which have significantly improved the clarity and quality of this work. KS acknowledges support from the Gordon and Betty Moore Foundation and the John Templeton Foundation via grants to the Black Hole Initiative at Harvard University. GLB acknowledges support from the NSF (AST-2108470 and AST-2307419, ACCESS), a NASA TCAN award, and the Simons Foundation through the Learning the Universe Collaboration. ZH acknowledges support from NSF grant AST-2006176. Numerical calculations were run on the Flatiron Institute cluster 'popeye' and 'rusty', Frontera with allocation AST22010, and Bridges-2 with Access allocations TG-PHY220027 and TG-PHY220047. This work was performed in part at Aspen Center for Physics, which is supported by National Science Foundation grant PHY-2210452. We also thank the FIRE and the LtU collaborations.

DATA AVAILABILITY

The data supporting the plots within this article are available on reasonable request to the corresponding author. A public version of

the GIZMO code is available at http://www.tapir.caltech.edu/~phopkins/Site/GIZMO.html.

REFERENCES

Abel T., Bryan G. L., Norman M. L., 2002, Science, 295, 93
Alvarez M. A., Wise J. H., Abel T., 2009, ApJ, 701, L133
Barai P., de Gouveia Dal Pino E. M., 2019, MNRAS, 487, 5549
Begelman M. C., Cioffi D. F., 1989, ApJ, 345, L21
Bennett J. S., Sijacki D., Costa T., Laporte N., Witten C., 2024, MNRAS, 527, 1033
Bîrzan L., Rafferty D. A., McNamara B. R., Wise M. W., Nulsen P. E. J., 2004, ApJ, 607, 800
Bourne M. A., Sijacki D., 2017, MNRAS, 472, 4707
Bradford J. D., Geha M. C., Greene J. E., Reines A. E., Dickey C. M., 2018, ApJ, 861, 50
Bromm V., Coppi P. S., Larson R. B., 1999, ApJ, 527, L5
Bromm V., Coppi P. S., Larson R. B., 2002, ApJ, 564, 23
Carnall A. C. et al., 2023, Nature, 619, 716
Cho H., Prather B. S., Narayan R., Natarajan P., Su K.-Y., Ricarte A., Chatterjee K., 2023, ApJ, 959, L22
Cho H., Prather B. S., Su K.-Y., Narayan R., Natarajan P., 2024, ApJ, 977, 200
Dickey C. M., Geha M., Wetzel A., El-Badry K., 2019, ApJ, 884, 180
Dubois Y., Devriendt J., Slyz A., Teyssier R., 2010, MNRAS, 409, 985
Fabian A. C., 2012, ARA&A, 50, 455
Gaspari M., Brighenti F., Temi P., 2012, MNRAS, 424, 190
Greene J. E., Ho L. C., Ulvestad J. S., 2006, ApJ, 636, 56
Guo M., Stone J. M., Quataert E., Kim C.-G., 2024, ApJ, 973, 141
Gürkan M. A., Freitag M., Rasio F. A., 2004, ApJ, 604, 632
Harikane Y. et al., 2023, ApJ, 959, 39
Hickox R. C., Alexander D. M., 2018, ARA&A, 56, 625
Hopkins P. F., 2015, MNRAS, 450, 53
Inayoshi K., Visbal E., Haiman Z., 2020, ARA&A, 58, 27
Kocevski D. D. et al., 2023, ApJ, 954, L4
Koudmani S., Sijacki D., Bourne M. A., Smith M. C., 2019, MNRAS, 484, 2047
Larson R. L. et al., 2023, ApJ, 953, L29
Li Y., Bryan G. L., 2014, ApJ, 789, 54
Li Y., Bryan G. L., Ruszkowski M., Voit G. M., O'Shea B. W., Donahue M., 2015, ApJ, 811, 73
Maiolino R. et al., 2024, Nature, 627, 59
Manzano-King C. M., Canalizo G., Sales L. V., 2019, ApJ, 884, 54
Massonneau W., Volonteri M., Dubois Y., Beckmann R. S., 2022, A&A, 670, A180
Mehta D., Regan J. A., Prole L., 2024, Open J. Astrophys., 7, 107
Mezcua M., Lobanov A. P., 2011, Astron. Nachr., 332, 379
Mezcua M., Farrell S. A., Gladstone J. C., Lobanov A. P., 2013a, MNRAS, 436, 1546
Mezcua M., Roberts T. P., Sutton A. D., Lobanov A. P., 2013b, MNRAS, 436, 3128
Mezcua M., Roberts T. P., Lobanov A. P., Sutton A. D., 2015, MNRAS, 448, 1893
Mezcua M., Civano F., Marchesi S., Suh H., Fabbiano G., Volonteri M., 2018a, MNRAS, 478, 2576
Mezcua M., Kim M., Ho L. C., Lonsdale C. J., 2018b, MNRAS, 480, L74
Mezcua M., Suh H., Civano F., 2019, MNRAS, 488, 685
Milosavljević M., Bromm V., Couch S. M., Oh S. P., 2009, ApJ, 698, 766
Nyland K., Marvil J., Wrobel J. M., Young L. M., Zauderer B. A., 2012, ApJ, 753, 103
Nyland K. et al., 2017, ApJ, 845, 50
Onoue M. et al., 2023, ApJ, 942, L17
Pacucci F., Nguyen B., Carniani S., Maiolino R., Fan X., 2023, ApJ, 957, L3
Park K., Ricotti M., 2011, ApJ, 739, 2
Penny S. J. et al., 2018, MNRAS, 476, 979
Portegies Zwart S. F., McMillan S. L. W., 2002, ApJ, 576, 899
Prasad D., Sharma P., Babul A., 2015, ApJ, 811, 108
Regan J., Volonteri M., 2024, Open J. Astrophys., 7, 72
Regan J. A., Downes T. P., Volonteri M., Beckmann R., Lupi A., Trebitsch M., Dubois Y., 2019, MNRAS, 486, 3892
Reines A. E., Deller A. T., 2012, ApJ, 750, L24
Reines A. E., Plotkin R. M., Russell T. D., Mezcua M., Condon J. J., Sivakoff G. R., Johnson K. E., 2014, ApJ, 787, L30
Reines A. E., Condon J. J., Darling J., Greene J. E., 2020, ApJ, 888, 36
Ruszkowski M., Yang H.-Y. K., Zweibel E., 2017, ApJ, 834, 208
Ryu T., Tanaka T. L., Perna R., Haiman Z., 2016, MNRAS, 460, 4122
Sbarrato T., Ghisellini G., Giovannini G., Giroletti M., 2021, A&A, 655, A95
Sbarrato T., Ghisellini G., Tagliaferri G., Tavecchio F., Ghirlanda G., Costamante L., 2022, A&A, 663, A147
Schleicher D. R. G., Galli D., Glover S. C. O., Banerjee R., Palla F., Schneider R., Klessen R. S., 2009, ApJ, 703, 1096
Schneider R., Valiante R., Trinca A., Graziani L., Volonteri M., Maiolino R., 2023, MNRAS, 526, 3250
Scoggins M. T., Haiman Z., 2024, MNRAS, 531, 4584
Sethi S., Haiman Z., Pandey K., 2010, ApJ, 721, 615
Shakura N. I., Sunyaev R. A., 1973, A&A, 500, 33
Sharma R. S., Brooks A. M., Somerville R. S., Tremmel M., Bellovary J., Wright A. C., Quinn T. R., 2020, ApJ, 897, 103
Shi Y., Grudić M. Y., Hopkins P. F., 2021, MNRAS, 505, 2753
Su K.-Y. et al., 2020, MNRAS, 491, 1190
Su K.-Y. et al., 2021, MNRAS, 507, 175
Su K.-Y. et al., 2023a, MNRAS, 532, 2724
Su K.-Y., Bryan G. L., Haiman Z., Somerville R. S., Hayward C. C., Faucher-Giguère C.-A., 2023b, MNRAS, 520, 4258
Su K.-Y. et al., 2024, MNRAS, 532, 2724
Takeo E., Inayoshi K., Mineshige S., 2020, MNRAS, 497, 302
Torrey P. et al., 2020, MNRAS, 497, 5292
Turk M. J., Oishi J. S., Abel T., Bryan G. L., 2012, ApJ, 745, 154
Übler H. et al., 2023, A&A, 677, A145
Webb N. et al., 2012, Science, 337, 554
Weinberger R. et al., 2023, MNRAS, 523, 1104
Wellons S. et al., 2022, MNRAS, 520, 5394
Wrobel J. M., Ho L. C., 2006, ApJ, 646, L95
Wrobel J. M., Greene J. E., Ho L. C., Ulvestad J. S., 2008, ApJ, 686, 838
Yang H.-Y. K., Reynolds C. S., 2016, ApJ, 818, 181
Yang H. Y. K., Sutter P. M., Ricker P. M., 2012, MNRAS, 427, 1614

This paper has been typeset from a TEX/LATEX file prepared by the author.